

## Mean Motion Resonances in AGN Disks

MARGUERITE EPSTEIN-MARTIN  <sup>1</sup>, NICHOLAS STONE  <sup>2,3</sup> AND JULIETTE BECKER  <sup>2</sup>

<sup>1</sup>*Department of Astronomy, Columbia University, 550 West 120th Street, New York, NY 10027, USA*

<sup>2</sup>*Department of Astronomy, University of Wisconsin-Madison, Madison, WI 53706*

<sup>3</sup>*Racah Institute of Physics, The Hebrew University, Jerusalem, 91904, Israel*

### ABSTRACT

Mean motion resonances (MMRs) are a generic outcome of convergent migration for bodies embedded in accretion disks around a central mass. Long studied in planetary systems, the same phenomenon should occur for stellar-mass black holes (BHs) in AGN disks. In this work, we derive simple analytic criteria describing when BH pairs are driven out of resonance, and use them to chart MMR stability across AGN parameter space, accounting for disruption from general-relativistic apsidal precession, hydrodynamic turbulence, and stellar stirring. Across plausible AGN disk models, we find three MBH mass regimes: (i) for  $M/M_{\odot} \gtrsim 10^{7.5}$ , first order resonances are generically unstable; (ii) for  $M/M_{\odot} \lesssim 10^{6.5}$ , stable MMRs are always present; (iii) for  $10^{6.5} \lesssim M/M_{\odot} \lesssim 10^{7.5}$ , stability depends on disk mass flux, the summed mass of the orbiters, and the nuclear-cusp slope. When present, stable MMRs commonly occur between an inner anti-trap and an outer trap set by thermal torque, a region where embedded objects migrate outward in the disk. These results imply that high-mass AGN allow convergent migration to proceed to LVK-band mergers largely without resonant chains, whereas low/intermediate-mass AGN can host MMRs, with the potential to reshape merger pathways.

### 1. INTRODUCTION

The groundbreaking discovery of gravitational waves (GWs) by Advanced LIGO in 2015 inaugurated a new era in high energy astrophysics (B. P. Abbott et al. 2016). Since the first observed compact binary merger, the LIGO-Virgo-KAGRA (LVK) collaboration has published over 200 additional GW signals (R. Abbott et al. 2023; The LIGO Scientific Collaboration et al. 2025), the overwhelming majority of which are from binary mergers of stellar mass black holes (BHs). In contrast to the small minority of binary neutron star mergers, whose event rates and origins had been pre-calibrated by short gamma ray bursts (D. M. Coward et al. 2012), the detection of so many binary BHs came as a surprise.

A decade later, there is still no consensus on the astrophysical origins of the LVK BH mergers, and half a dozen scenarios still contend to explain this population. These scenarios can be broken into roughly three categories. First: isolated binary evolution channels, such as a common envelope phase (A. V. Tutukov & L. R. Yungelson 1993; K. Belczynski et al. 2016), chemically homogeneous evolution following tidal synchronization (I. Mandel & S. E. de Mink 2016), or stable mass transfer (L. A. C. van Son et al. 2022). Second: vacuum

gravitational dynamics channels, such as chaotic 3-body scatterings in dense star clusters (S. F. Portegies Zwart & S. L. W. McMillan 2000; C. L. Rodriguez et al. 2016), or Kozai-Lidov cycles in hierarchic triples (F. Antonini & H. B. Perets 2012; F. Antonini et al. 2017). In this paper, we focus on the third type of binary BH origin: hydrodynamic assembly and merger of binaries in the gas-rich environments of active galactic nuclei, or AGN (B. McKernan et al. 2014; J. M. Bellovary et al. 2016; N. C. Stone et al. 2017; I. Bartos et al. 2017).

In the “AGN channel” for binary BH mergers, there are multiple ways for the BH binaries to assemble. They may be formed *in situ* via Toomre instability (N. C. Stone et al. 2017), they may be captured by gas drag (I. Bartos et al. 2017) from a pre-existing binary population in the nuclear star cluster (NSC), or they may be assembled via single-single capture within the AGN disk itself. These single-single captures are mediated by various forms of dissipation (H. Tagawa et al. 2020; C. Rowan et al. 2023; Y. Wang et al. 2024) during close passages between isolated BHs. BHs embedded in the AGN typically move on quasi-circular orbits<sup>4</sup>, so these close passages require *convergent migration*.

<sup>4</sup> The minority of BHs embedded on retrograde orbits are an exception to this (A. Secunda et al. 2021).

Protoplanetary disk bearing systems offer a useful analogue to the AGN channel (B. McKernan et al. 2012). Exchange of angular momentum between embedded planets and the gaseous disk leads to planetary migration (P. Goldreich & S. Tremaine 1980); the exact same forms of gravito-hydrodynamical angular momentum transport lead to BH migration in AGN. Migration rates are mass-dependent (S.-J. Paardekooper et al. 2013), so BHs of different masses may overtake one another, setting the stage for single-single capture. This can occur in the bulk of the disk, or alternatively at special locations known as migration traps, where the sign of the migration torque flips and a region of inward migration sits exterior to one of outward migration (J. M. Bellovary et al. 2016). Regardless, AGN disk conditions that favor single-single capture will likely lead to large enhancements in the LVK merger rate (relative to AGN channel mergers limited to primordial binaries), along with the tantalizing possibility of hierarchical mergers and BH growth into the pair instability mass gap (Y. Yang et al. 2019; H. Tagawa et al. 2021).

Further consideration of the analogy between protoplanetary and AGN disks also leads to an equivalent AGN channel for extreme mass ratio inspirals, or EMRIs (P. Amaro-Seoane 2018). EMRIs are a future class of GW sources produced when a stellar mass compact object (typically but not necessarily a BH) inspirals into a massive black hole in a galactic nucleus. EMRI waveforms do not extend to the high GW frequencies observable by the LVK collaboration, but would be visible to space-based GW interferometers like the future *LISA* (P. Amaro-Seoane et al. 2023) or *Taiji/TianQin* (J. Luo et al. 2016; W.-H. Ruan et al. 2020) missions. While most theoretical calculations of EMRI formation focus on scattering of BHs onto high eccentricity “loss cone” orbits (C. Hopman & T. Alexander 2005), orbital migration may lead to “wet EMRI” production in AGN disks (Y. Levin 2007; Z. Pan & H. Yang 2021). These wet EMRIs would have relatively unique signatures (Z. Pan et al. 2022) and may even dominate overall EMRI rates (Z. Pan et al. 2021; A. Derdzinski & L. Mayer 2023), but their properties depend on outcomes of AGN migration.

In planetary systems, convergent migration frequently leads to mean motion commensurabilities, and capture into mean motion resonance (MMR). Within our own solar system, Jupiter and Saturn may have once occupied a resonant state (A. Morbidelli & A. Crida 2007), before undergoing instabilities that drove orbits to their current locations (K. Batygin & M. E. Brown 2010). Likewise, R. Malhotra (1995) proposed that this process may have been the origin of the 3:2 MMR between Neptune and Pluto. The prevalence of planetary MMRs is

understood to result from dissipative migration. Across a significant swath of parameter space, migration among planetary pairs is expected to be slow and convergent, essentially guaranteeing capture into resonance (J. Henrard 1982). Given the importance of migration for GW production in AGN, it is therefore logical to consider under what conditions MMRs may emerge for embedded BHs.

The few-body numerical integrations of A. Secunda et al. (2019, 2020) have demonstrated that stellar mass BHs can indeed capture into MMR while migrating towards traps in AGN disks<sup>5</sup>. However, even in circumstances where resonant capture is likely, the strength and stability of resonances in the dynamically complex environment of an AGN disk is an open question. In analogous protoplanetary systems, gaseous turbulence is capable of destabilizing MMRs (S.-J. Paardekooper et al. 2013; F. C. Adams et al. 2008; K. Batygin & F. C. Adams 2017). The probability of permanent capture into resonance can also be reduced by slightly non-axisymmetric disk potentials (K. Batygin 2015). And K. M. Deck & K. Batygin (2015) illustrated that resonant metastability depends on the competing timescales for migration and eccentricity damping. Other sources of instability, absent from the protoplanetary context, may emerge for BHs in MMR in AGN: for example, weak gravitational perturbations from stars in the disk or the surrounding NSC (N. C. Stone et al. 2017), or the increased importance of general relativistic effects near the MBH (N. Seto & T. Muto 2010).

In this paper, we systematically explore the landscape of MMR stability in AGN disks. We employ analytic methods so as to survey the broad parameter space of AGN, which can vary by many orders of magnitude in MBH mass and gas accretion rate. In §2, we develop a resonant Hamiltonian that describes the underlying dynamics of the problem. In §3, we review the relevant physical processes governing the migration of embedded BHs in AGN. In §4, we explore the physics of three different physical effects – relativistic precession, hydrodynamical turbulence, and stellar scattering – that may each act to destabilize MMRs in AGN disks. In §5, we assemble general criteria for resonance disruption. In §6, we present our parameter space exploration of MMR stability, and discuss the implications of these results for

<sup>5</sup> More recent works have also found evidence for the capture of stellar mass BHs into MMR with *intermediate mass* BHs migrating inwards due to either GW emission (O. Reved et al. 2025) or gas torques (P. Peng et al. 2025), although we do not consider intermediate mass BH secondaries in this paper.

GW production. Finally, in §7, we conclude with a summary of our main findings.

## 2. MEAN MOTION RESONANCES: SET-UP OF THE INTEGRABLE PROBLEM

We begin our analysis by introducing the integrable approximation for first-order resonant motion (i.e. the orbital period ratio of  $P_1/P_2 \simeq (k+1)/k$ ). This approach has been widely used in the planetary dynamics literature (e.g. [W. Sessin & S. Ferraz-Mello \(1984\)](#); [K. Batygin & A. Morbidelli \(2013\)](#); [K. M. Deck & K. Batygin \(2015\)](#)) but is less common in the context of AGN, although their geometries are analogous. The system of interest includes two coplanar, embedded objects of mass  $m_1$  and  $m_2$  orbiting a central mass  $M$ , with periods near the first order ratio,  $k+1:k$ . In this regime, the Hamiltonian can be approximated as,

$$\mathcal{H} = -\frac{GMm_1}{2a_1} - \frac{GMm_2}{2a_2} - \frac{Gm_1m_2}{a_2} \times [f_{k+1,27}(\alpha)e_1 \cos(\theta - \varpi_1) + (f_{k+1,31}(\alpha) - 2\delta_{k,1}\alpha)e_2 \cos(\theta - \varpi_2)], \quad (1)$$

where  $\theta = (k+1)\lambda_2 - k\lambda_1$  is the resonant angle, and  $a_i$ ,  $e_i$ ,  $\lambda_i$ , and  $\varpi_i$  are the semi-major axes, eccentricity, mean longitudes, and longitudes of periaxis of the orbiters. The quantities  $f_{k+1,27}$  and  $f_{k+1,31}$  are dimensionless functions of Laplace coefficients ([C. D. Murray & S. F. Dermott 1999](#)) evaluated at  $\alpha \equiv a_1/a_2$ . At the resonance center,  $a_1 = [k/(k+1)]^{2/3}a_2$ . Expanding around this equilibrium point allows us to approximate our coefficients as functions of  $k$ ,

$$\begin{aligned} f_{k+1,27} &\approx -0.8k \\ f_{k+1,31} &\approx 0.8k, \end{aligned} \quad (2)$$

as shown in [A. C. Quillen \(2011\)](#). Finally, the term including the Kronecker delta function,  $\delta_{k,1}$ , comes from the indirect part of the disturbing function.

Keplerian orbital elements are not canonical, so we transform Equation (1) into Poincaré action-angle variables:

$$\begin{aligned} \Lambda_i &= m_i \sqrt{GMa_i} & \lambda_i &= \Omega_i + \omega_i + M_i \\ \Gamma_i &= \Lambda_i \left(1 - \sqrt{1 - e_i^2}\right) \approx \Lambda_i \frac{e_i^2}{2} & \gamma_i &= -\varpi_i \end{aligned} \quad (3)$$

where, under the assumption of nearly circular orbits, we have approximated  $\Gamma_i \propto e_i^2$ . The Keplerian and resonant components of the Hamiltonian are re-written as

$$\mathcal{H}_{\text{kep}} = -\frac{G^2 M^2 m_1^3}{2\Lambda_1^2} - \frac{G^2 M^2 m_2^3}{2\Lambda_2^2} \quad (4)$$

$$\begin{aligned} \mathcal{H}_{\text{res}} = & -\frac{G^2 M m_1 m_2^3}{\Lambda_2^2} \left( f_{k+1,27} \sqrt{\frac{2\Gamma_1}{\Lambda_1}} \cos(\theta + \gamma_1) \right. \\ & \left. + f'_{k+1,31} \sqrt{\frac{2\Gamma_2}{\Lambda_2}} \cos(\theta + \gamma_2) \right), \end{aligned} \quad (5)$$

where we have defined  $f'_{k+1,31} \equiv f_{k+1,31} - 2\delta_{k,1}\alpha$  for simplicity.

Following the procedure laid out in [K. Batygin & A. Morbidelli \(2013\)](#), we further simplify the Hamiltonian by employing an additional canonical transformation using the action-angle variables

$$\begin{aligned} \mathcal{K} &= \Lambda_1 + \frac{k}{k+1} & \kappa &= \lambda_1, \\ \Theta &= \Lambda_2/(k+1) & \theta &= k\lambda_2 - (k-1)\lambda_1. \end{aligned} \quad (6)$$

We then expand the Hamiltonian around the nominal resonant location, carrying out the expansion to second order in  $\delta\Lambda_i = \Lambda_i - [\Lambda_i]$ , where  $[\Lambda_i] = m_i [n_i] [a_i^2]$  is the nominal resonance value and  $[n_i] = \sqrt{GM/[a_i]^3}$  is the nominal mean motion. Using the resonant relationship  $k[n_1] = (k+1)[n_2]$ , the Keplerian Hamiltonian becomes,

$$\begin{aligned} \mathcal{H}_{\text{kep}} = & 4[n_1] \mathcal{K} + 3k[h_1] \mathcal{K}\Theta - \frac{3}{2}\Theta^2 \\ & \times \left( [h_1] k^2 + [h_2] (k+1)^2 \right) - \frac{3}{2}\mathcal{K}^2 [h_1], \end{aligned} \quad (7)$$

where  $[h_i] = [n_i]/[\Lambda_i] = 1/(m_i [a_i]^2)$ . The resonant contribution to  $\mathcal{H}$  takes the form

$$\mathcal{H}_{\text{res}} = -\zeta \sqrt{2\Gamma_1} \cos(\gamma_1 + \theta) - \beta \sqrt{2\Gamma_2} \cos(\gamma_2 + \theta), \quad (8)$$

where the pre-factors  $\zeta$  and  $\beta$  are

$$\zeta = \frac{G^2 M m_1 m_2^3}{[\Lambda_2]^2} \frac{f_{k+1,27}}{\sqrt{[\Lambda_1]}} = \frac{f'_{k+1,31}}{f_{k+1,27}} \sqrt{\frac{[\Lambda_1]}{[\Lambda_2]}} \beta. \quad (9)$$

Critically,  $\kappa$  is no longer in  $\mathcal{H}$ , thus  $\mathcal{K}$  is a constant of motion and we can drop the first and last terms in  $\mathcal{H}_{\text{kep}}$ . We are left with three sets of conjugate coordinate pairs, too many for integrability.

The Hamiltonian can be reduced to a single degree of freedom by exploiting a symmetry in the resonant problem: to leading order, the disturbing function depends only on a linear combination of the eccentricity vectors of the original orbits ([S. Hadden 2019](#); [D. Tamayo & S. Hadden 2025](#)). In this sense, the geometry and dynamics are equivalent to the circular restricted case ([A. C. Quillen 2006](#)), with the test particle's eccentricity replaced by a generalized composite eccentricity. This much simpler coordinate system is defined by a canonical rotation (e.g. [W. Sessin & S. Ferraz-Mello 1984](#); [J.](#)

Wisdom 1986; K. Batygin & A. Morbidelli 2013), with associated action-angle coordinates:

$$\Phi = \frac{(\zeta^2 \Gamma_1 + \beta^2 \Gamma_2 + 2\zeta\beta\sqrt{\Gamma_1\Gamma_2} \cos(\gamma_1 - \gamma_2))}{\sqrt{\zeta^2 + \beta^2}}, \quad (10)$$

$$\phi = \arctan\left(\frac{\zeta\sqrt{2\Gamma_1} \sin \gamma_1 + \beta\sqrt{2\Gamma_2} \sin \gamma_2}{\zeta\sqrt{2\Gamma_1} \cos \gamma_1 + \beta\sqrt{2\Gamma_2} \cos \gamma_2}\right).$$

Re-written in terms of these coordinates, the Hamiltonian is reduced to a form that contains only a single harmonic

$$\mathcal{H} = 3k[h_1]\mathcal{K}\Theta - \frac{3}{2} \left( [h_1]k^2 + [h_2](k+1)^2 \right) \Theta^2 - \sqrt{\alpha^2 + \beta^2} \sqrt{2\Phi} \cos(\phi + \theta). \quad (11)$$

Employing a final contact transformation yields the action-angle variables

$$\begin{aligned} \Psi &= \Phi, & \psi &= \phi + \theta, \\ \Omega &= \Theta - \Psi, & w &= \theta. \end{aligned} \quad (12)$$

In these coordinates the Hamiltonian is independent of  $w$ , making  $\Omega$  the final conserved quantity. Our system is thus reduced to a single degree of freedom. Dropping constant terms, the Hamiltonian is recast in integrable form as:

$$\begin{aligned} \mathcal{H} &= -3([h_2](k+1)^2\Omega - k[h_1](\mathcal{K} - k\Omega))\Psi \\ &\quad - \frac{3}{2}([h_1]k^2 + [h_2](k+1)^2)\Psi^2 \\ &\quad - \sqrt{\zeta^2 + \beta^2}\sqrt{2\Psi} \cos(\psi). \end{aligned} \quad (13)$$

We can simplify this expression further by rescaling the actions by a constant factor  $\eta$ , chosen so that the coefficients of  $\Psi^2$  and  $\sqrt{2\Psi}$  are equal. This gives

$$\eta = \left( \frac{\zeta^2 + \beta^2}{9([h_1]k^2 + [h_2](k+1)^2)} \right)^{1/3}. \quad (14)$$

In the ‘compact-limit’ approximation – i.e.  $\langle a \rangle \equiv a_1 \simeq a_2$  (equivalently,  $k+1 \simeq k$ ) – the same rescaling can be written in terms of the masses as

$$\eta = \left( \frac{\zeta^2 \langle a \rangle^2 (m_1 + m_2)}{9m_2^5 m_1^2 (m_2 k^2 + m_1 (k+1)^2)^2} \right)^{1/3}. \quad (15)$$

This approximation agrees well with  $N$ -body integrations, particularly for  $k \geq 2$  (K. M. Deck et al. 2013). The re-scaled actions are defined

$$\tilde{\mathcal{H}} = \mathcal{H}/\eta \quad \tilde{\Psi} = \Psi/\eta \quad \tilde{\mathcal{K}} = \mathcal{K}/\eta \quad \tilde{\Omega} = \Omega/\eta. \quad (16)$$

By choosing to measure time in units of  $3m_1m_2(m_2k^2 + m_1(1+k)^2)/(2\langle a \rangle)$ , we divide  $\mathcal{H}$  by the same factor and obtain

$$\mathcal{H} = 3(\delta + 1)\tilde{\Psi} - \tilde{\Psi}^2 - 2\sqrt{2\tilde{\Psi}} \cos(\psi). \quad (17)$$

Although cumbersome to derive, Equation (17) has the form of the second fundamental model of resonance as described in J. Henrard & A. Lemaitre (1983). The phase-space morphology is governed entirely by the resonant proximity parameter  $\delta$ . For  $\delta < 0$  the system behaves like a forced harmonic oscillator, with circulating  $\psi$ . When  $\delta \geq 0$ , the system is pendulum-like, and librates within the emergent, resonant island.

Following K. Batygin & F. C. Adams (2017), it is useful to define the Hamiltonian variables in terms of physical quantities:  $\delta$  is

$$\delta = \frac{2}{3} \left( \frac{15}{4} \frac{kM}{m_1 + m_2} \right)^{2/3} \left( \sigma^2 - \frac{\Delta\alpha}{k} \right) \quad (18)$$

where  $\Delta\alpha = \Delta(a_1/a_2)$  denotes the deviation of the semimajor-axis ratio from its nominal resonant value. And the action-angle coordinates are

$$\begin{aligned} \tilde{\Psi} &= \sigma_c \left( \frac{15}{4} \frac{kM}{m_1 + m_2} \right)^{2/3}, \\ \psi &= (k+1)\lambda_2 - k\lambda_1 - \varpi_c, \end{aligned} \quad (19)$$

where the composite eccentricity  $\sigma_c$  and generalized longitude of periaxis  $\varpi_c$  are defined by

$$\sigma_c = \sqrt{e_1^2 + e_2^2 + 2e_1e_2 \cos(\varpi_1 - \varpi_2)}, \quad (20)$$

and

$$\varpi_c = \arctan \left[ \frac{e_2 \sin \varpi_2 + e_1 \sin \varpi_1}{e_1 \cos \varpi_1 + e_2 \cos \varpi_2} \right]. \quad (21)$$

The evolution of the resonant system is now fully specified given quantities  $M$ ,  $m_1 + m_2$ ,  $k$ ,  $e_{1,2}$  and  $\varpi_{1,2}$ . Notably, the mass dependence of the orbiters enters only through their sum ( $m_1 + m_2$ ). This mass-symmetry is a consequence of the compact-limit reduction (K. Batygin & F. C. Adams 2017) and usefully collapses the parameter space, as systems with the same  $m_1 + m_2$  are dynamically equivalent.

## 2.1. Mean Motion Resonance under General Relativistic Precession

The classic 1PN GR Hamiltonian describes the precession in  $\omega$  due to general relativity (D. L. Richardson & T. J. Kelly 1988; F. C. Adams & G. Laughlin 2006; C. Migaszewski & K. Goździewski 2009; M. Volpi & A.-S. Libert 2024). This Hamiltonian can be written as

$$\mathcal{H}_{1PN} = -\frac{3G^2 M^2 m_i}{a_i^2 c^2 \sqrt{1 - e_i^2}}, \quad (22)$$

where  $c$  is the speed of light. Following Equation (22), we can write the precession rate of a low-eccentricity planetary orbit due to GR:

$$\dot{\omega}_{\text{GR}} = \frac{3(GM)^{3/2}}{a_i^{5/2} c^2}. \quad (23)$$

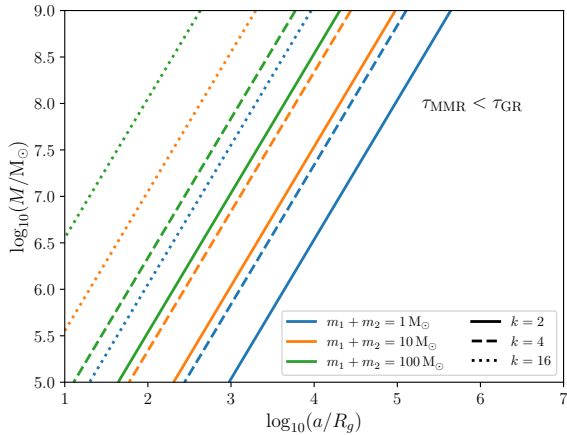


**Figure 1.** The boundary  $\dot{\omega}_{\text{MMR}}/\Delta\dot{\omega}_{\text{GR}} \approx 1$ , which separates the interior parameter space where GR dominates the dynamics (and the resonance is broken) from the exterior region where GR precession is sufficiently weak that the MMR can exist. Colors denote different masses for the inner object participating in the resonance, and line-styles denote the harmonic  $k$  in the  $k+1 : k$  first-order resonance. Higher harmonics shift the GR disruption boundary to smaller semi-major axes  $a$  by reducing the *differential* relativistic apsidal precession  $\Delta\dot{\omega}_{\text{GR}}$  between a resonant pair.

For two planets near a first order MMR (with period ratio  $k+1 : k$ ), with a Hamiltonian defined by Equation (7), the relevant GR frequency will be the differential precession, defined as

$$\Delta\dot{\omega}_{\text{GR}} = |\dot{\omega}_{\text{GR},1} - \dot{\omega}_{\text{GR},2}| \quad (24)$$

$$\approx \frac{3(GM)^{3/2}}{c^2 a_1^{5/2}} \left( 1 - \left( \frac{k+1}{k} \right)^{-5/3} \right) \quad (25)$$

Following Equation (5), the libration frequency of the resonance will be (C. D. Murray & S. F. Dermott 1999):

$$\dot{\omega}_{\text{MMR}} = \frac{3[n_2]}{2} \left( \frac{M}{m_1 + m_2} \right)^{-2/3} \left[ \frac{(3f_{k+1,27})^{-1/3}}{((k+1)^5(k))^{1/9}} \right]^{-1}. \quad (26)$$

When  $\dot{\omega}_{\text{MMR}}/\Delta\dot{\omega}_{\text{GR}} \approx 1$ , precession due to GR will be commensurate with MMR libration, and the resonance will break. In Figure 1, we plot the boundaries in the  $\log_{10}(a/R_G)$ – $\log_{10}(M/M_\odot)$  parameter space, where  $R_g \equiv GM/c^2$  is the gravitational radius of the MBH. The contours in Figure 1 separate the regions where the dynamics are dominated by general relativistic precession versus those dominated by MMR libration. For larger central masses  $M$  and less massive resonant objects  $m_i$ , GR tends to dominate the dynamics to more distant radii, pushing outwards the region where stable MMRs can persist.

Notably, these boundaries shrink to smaller radii when considering higher harmonics  $k$  of the first order MMR: as we can see from Equation 25, as  $k \rightarrow \infty$ , the *differential* apsidal precession rate  $\Delta\dot{\omega}_{\text{GR}} \rightarrow 0$ . This effect favors the survival of high MMR harmonics at small radii, although beyond some ( $e$ -dependent) value of  $k$ , resonance overlap will act on its own to destabilize these high harmonics.

### 3. MIGRATION

We anticipate that in AGN disks, as in their planetary system analogues, the dynamics described in the previous section will be modulated by the exchange of angular momentum and orbital energy between the embedded secondaries and the surrounding disk. One such exchange occurs via local excitation of spiral density waves (P. Goldreich & S. Tremaine 1979). Torque from the over-dense waves interior and exterior to the embedded object do not precisely cancel (W. R. Ward 1997), resulting in a residual net torque (S. J. Paardekooper et al. 2010) of

$$\Gamma_I = C_I \frac{H}{a} \Gamma_0, \quad (27)$$

where  $\Gamma_0$  is the approximate magnitude of the torque from a single spiral arm,

$$\Gamma_0 = \left( \frac{m}{M} \right)^2 \Sigma a^4 n^2 \left( \frac{H}{a} \right)^{-3}. \quad (28)$$

The variables  $H$  and  $\Sigma$  represent the scale height and surface density of the disk, respectively, and  $n$  is the Keplerian frequency at a given distance  $a$  from the MBH. The dimensionless pre-factor  $C_I$  is usually of order unity, and depends on disk density and temperature gradients. Recent calibrations from 3D hydrodynamical simulations (M. A. Jiménez & F. S. Masset 2017) give

$$\Gamma_I = \left[ C_L + \left( 0.46 + 0.96 \frac{d \ln \Sigma}{d \ln a} - 1.8 \frac{d \ln T}{d \ln a} \right) \gamma^{-1} \right] \frac{H}{a} \Gamma_0. \quad (29)$$

In Equation (29),  $\gamma$  is the adiabatic index and  $C_L$ , the Lindblad torque prefactor (other dimensionless terms in Equation 29 encode the corotation torque), is given by (M. A. Jiménez & F. S. Masset 2017):

$$C_L = \left( -2.34 - 0.1 \frac{d \ln \Sigma}{d \ln a} + 1.5 \frac{d \ln T}{d \ln a} \right) f_\gamma(x). \quad (30)$$

The function  $f_\gamma$  interpolates between the locally isothermal and adiabatic limits of disk thermodynamics,

$$f_\gamma(x) = \frac{(x/2)^{1/2} + 1/\gamma}{(x/2)^{1/2} + 1} \simeq \begin{cases} \frac{1}{\gamma}, & x \ll 1, \\ 1, & x \gg 1. \end{cases} \quad (31)$$

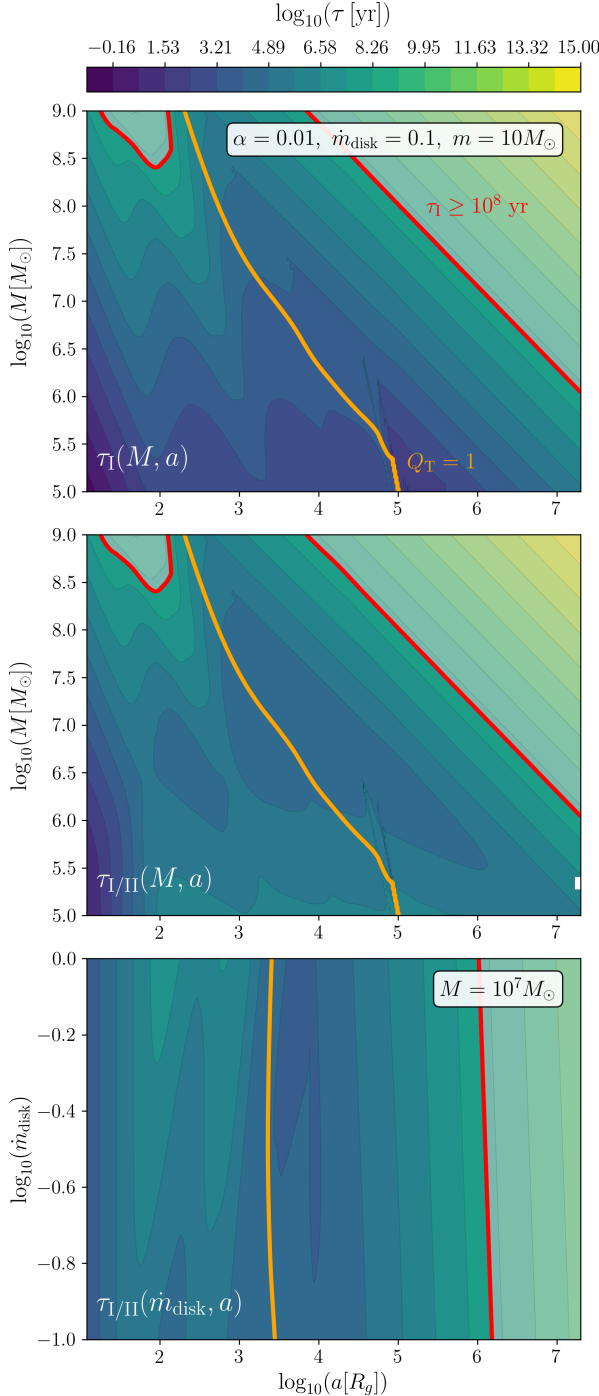


**Figure 2.** Colored contours show the migration timescale  $\tau$  as a function of distance from the MBH ( $a/R_g$ ) and disk parameters. The red curve marks  $\tau = 10^8$  yr, the maximum AGN lifetime. *Top panel:*  $\tau_I$  assuming Type I migration only, with  $\alpha_{\text{disk}} = 0.01$ ,  $\dot{m}_{\text{disk}} = 0.1$  (the disk mass flux in units of the Eddington rate), and a migrating mass  $m = 10 M_\odot$ . *Middle panel:*  $\tau_{I/II}$  computed from Equation (35), i.e., the Type-I rate rescaled by the local surface density; both top and middle panels vary the central mass  $M$ . *Bottom panel:*  $\tau_{I/II}$  as a function of  $\dot{m}_{\text{disk}}$  and  $a/R_g$  for fixed  $M = 10^7 M_\odot$ . The orange line indicates the minimum radius where marginal stability is imposed; to the right of this line the E. Sirkov & J. Goodman (2003) models assume stellar feedback maintains  $Q_T = 1$ .

Here the dimensionless variable  $x \equiv \chi/(H^2 n)$  is the ratio of thermal diffusivity ( $\chi$ ) to  $H^2 n$ , and  $x \ll 1$  ( $x \gg 1$ ) limits represent adiabatic (isothermal) disk conditions. Under the assumption of heat transport by optically thick radiative diffusion, the thermal diffusivity is

$$\chi = \frac{16\gamma(\gamma-1)\sigma_{\text{sb}}T^4}{3\kappa\rho^2H^2n^2}, \quad (32)$$

where  $\sigma_{\text{sb}}$  is the Stefan-Boltzmann constant and  $T$ ,  $\rho$ , and  $\kappa$  are the local temperature, density, and opacity of the AGN disk.

In the AGN context, we must also account for gravitational-wave (GW) emission from the compact secondary's orbital motion around the MBH. Unlike in planetary systems, where GR effects manifest – at most – as a conservative form of precession, embedded objects in AGN disks can reach radii where GW back-reaction is dynamically competitive with, and eventually dominates over, gas torques. The GW torque contribution can be expressed in fractional form as

$$\frac{\Gamma_{\text{GW}}}{\Gamma_0} = \frac{32}{5} \left( \frac{R_g}{a} \right)^{5/2} \left( \frac{H}{a} \right)^3 \frac{M}{\Sigma a^2} \quad (33)$$

where we have assumed a quasi-circular inspiral (P. C. Peters 1964). The GW torque is strictly negative (i.e. causing inward migration) and grows rapidly at small radii,  $\Gamma_{\text{GW}}/\Gamma_0 \propto (a/R_g)^{-6}$ . Because  $\Gamma_{\text{GW}}$  itself is set by the binary dynamics (i.e. it is independent of disk hydrodynamics) we can combine it linearly with  $\Gamma_I$  to get a total torque  $\Gamma_I + \Gamma_{\text{GW}}$ . For the rest of this paper, we include the GW torque contribution implicitly whenever we calculate migration torques and corresponding timescales.

Here we convert torque into a radial migration timescale  $\tau_I$  by balancing orbital angular momentum ( $\Lambda$ ) against applied torque  $\Gamma_I$ ,

$$\tau_I = \frac{\Lambda}{\Gamma_I} = \frac{1}{2n} \frac{M^2}{m \Sigma a^2} \left( \frac{H}{a} \right)^3 \left| \frac{\Gamma_I}{\Gamma_0} \right|. \quad (34)$$

The Type-I prescription is appropriate for low-mass orbiters that do not appreciably perturb the local disk. However, a massive object can partially deplete the gas near its orbit, lowering the effective surface density and reducing its coupling to the local disk. This regime is known as Type II migration (D. N. C. Lin & J. Papaloizou 1986). In the classic Type II picture, a sufficiently massive object opens a gap in the disk and local angular momentum exchange stops; the embedded object instead locks to the viscous evolution of the disk itself. However, hydrodynamic simulations (P. C. Duffell et al. 2014; K. D. Kanagawa et al. 2018)

have shown that even when the torque from an embedded object exceeds the viscous torque of the gas, some gas leaks through the gap. The resulting migration timescale, even for a massive migrator, is thus given by the Type I migration timescale scaled by a reduced surface density  $\Sigma_{\min} = \Sigma/(1 + 0.04K)$ , where  $K = (\frac{m}{M})^2 (\frac{H}{a})^{-5} \alpha_{\text{disk}}^{-1}$  (K. D. Kanagawa et al. 2018) and  $\alpha_{\text{disk}} < 1$  is the Shakura-Sunyaev disk viscosity parameter (N. I. Shakura & R. A. Sunyaev 1973). The migration timescale for low and high mass orbiters is parameterized by a smooth transition from the unperturbed, Type I limit ( $K \ll 1$ ) to the deep gap limit ( $K \gg 1$ ) according to the equation

$$\tau_{\text{I/II}} = \frac{\Sigma}{\Sigma_{\min}} \tau_{\text{I}}. \quad (35)$$

In order to evaluate the torques and migration timescales, we must adopt a disk model to supply the local thermodynamic and structural gradients. The classic, steady state  $\alpha$ -disk is known to break down in the outer regions of AGN, becoming unstable to self-gravity (I. Shlosman & M. C. Begelman 1989). To prevent runaway fragmentation and disk depletion, many AGN disk models invoke self-limiting star formation, whose feedback regulates the disk. The stability of the disk is represented by the Toomre parameter  $Q_{\text{T}}$  (A. Toomre 1964), where  $Q_{\text{T}} < 1$  indicates instability. Two widely used frameworks are E. Sirk & J. Goodman (2003) and T. A. Thompson et al. (2005) which construct modified viscous disks by requiring the disk maintain minimum marginal stability and setting  $Q_{\text{T}} = 1$ . These models differ most significantly in how they treat mass transport: T. A. Thompson et al. (2005) allow  $\dot{M}_{\text{disk}}$  to vary with radius in response to *in situ* star formation, whereas E. Sirk & J. Goodman (2003) enforce a steady inflow rate. Although the T. A. Thompson et al. (2005) model may be more physically motivated, here we adopt the E. Sirk & J. Goodman (2003) model so that we can investigate dependence on  $\dot{M}_{\text{disk}}$  explicitly. With this choice, we are able to generate the heat maps in Figure 2 using the pAGN package (D. Gangardt et al. 2024).

Figure 2 shows the migration timescales as contour maps:  $\tau_{\text{I}}$  (top panel) and  $\tau_{\text{I/II}}$  (middle and bottom panels). The top panel shows timescales in the  $(M, a)$  plane, adopting  $m = 10 M_{\odot}$ ,  $\alpha_{\text{disk}} = 0.01$ , and a disk mass accretion rate  $\dot{m}_{\text{disk}} = 0.1$  where  $\dot{m}_{\text{disk}} = \dot{M}_{\text{disk}}/\dot{M}_{\text{Edd}}$  is the dimensionless ratio of the disk mass flux over the Eddington rate,  $\dot{M}_{\text{Edd}} = L_{\text{Edd}}/c^2\eta$ , where  $L_{\text{Edd}} = 4\pi GcM/\kappa_e$  is the Eddington luminosity,  $\kappa_e \simeq 0.34 \text{ cm}^2 \text{ g}^{-1}$  is the electron scattering opacity, and  $\eta = 0.1$  is the radiative efficiency. The middle panel shows  $\tau_{\text{I/II}}$  in the same  $(M, a)$  plane and with the same system

parameters. In the bottom panel,  $\tau_{\text{I/II}}$  is plotted in the  $(\dot{m}_{\text{disk}}, a)$  plane, at fixed MBH mass  $M = 10^7 M_{\odot}$ , again with  $\alpha_{\text{disk}} = 0.01$ . The primary difference between the top and middle panels arises near  $\log_{10}(M/M_{\odot}) \simeq 5$ , where  $\tau_{\text{I/II}}$  is markedly longer than the corresponding  $\tau_{\text{I}}$ . This occurs because the gap parameter  $K \propto (m/M)^2$  becomes non-negligible at fixed  $m$  as  $M$  decreases. We also mark in red where the migration time reaches the upper limit of a typical disk lifetime  $t_{\text{AGN}} \sim 10^8 \text{ yr}$  (P. Martini & D. H. Weinberg 2001), and gray out regions with  $\tau > t_{\text{AGN}}$ ; systems in these zones are not expected to undergo significant migration-driven evolution in a single AGN episode.

In all panels in Figure 2, an orange line marks the innermost radius where marginal stability ( $Q_{\text{T}} = 1$ ) is invoked. To the right of this line, the E. Sirk & J. Goodman (2003) model that we use explicitly assumes that disk stability is maintained by stellar feedback. We flag this region because its structure depends on poorly constrained parameters and physical assumptions. In particular, the mass, number density, and type of embedded objects necessary to stabilize the outer AGN disk remains an open question (S. Gilbaum & N. C. Stone 2022; M. Epstein-Martin et al. 2025) – with consequences for the structure of the disk and anticipated migration torques. We discuss these uncertainties in more detail in §6.2.

Convergent migration is a necessary precondition for capture into MMRs. In the three panels of Figure 2, convergent drift for equal-mass pairs is confined to radii of  $\sim 10^2$  or  $10^4 R_{\text{g}}$ . This does not preclude convergence for unequal-mass pairs. Because  $\tau_{\text{I}} \propto m^{-1}$ , a sufficiently high mass body migrates faster and can overtake a lower mass body on an initially interior orbit. This dynamic holds true in the  $\tau_{\text{I/II}}$  case unless  $K \gg 1$  (i.e. deep gap regime), at which point migration rates decrease with increased object mass. However, once we incorporate thermal torques, the net torque can reverse sign and produce stable zero-torque zones: migration traps. These traps enforce convergence: objects outside the trap drift inward while those inside drift outward, so bodies of any mass are funneled toward the same radius.<sup>6</sup> We discuss the thermal torque prescription in the next section.

<sup>6</sup> Here we assume that convergent migration suffices for resonance capture. In fact, both convergence and adiabatic migration are required: the migration timescale must exceed the resonance libration period. See K. Batygin (2015), their Equation (43), for the adiabatic criterion. Assessing this constraint for AGN disks is an important task that we defer to future work. During the completion of this paper, we became aware of a parallel investigation that is examining the question of adiabaticity more carefully (Moncrieff & Grishin *in prep*).

### 3.1. Thermal Torques and Migration Traps

In addition to the gravitational perturbations associated with Type I/II torques, embedded objects perturb the temperature of local gas, which alters its density profile and creates gravitational back-reaction. F. S. Masset (2017b) formalized the resulting ‘thermal torque’ using linear theory, with analytic predictions that agree with simulations (E. Lega et al. 2014; P. Benítez-Llambay et al. 2015; O. Chrenko et al. 2017; A. M. Hankla et al. 2020). In the F. S. Masset (2017b) framework, the thermal response is governed by two quantities: (i) the diffusion length  $\lambda$ , which sets how far temperature perturbations spread under finite thermal diffusivity,

$$\lambda = \sqrt{\frac{2\chi}{3\gamma n}}; \quad (36)$$

and (ii) the co-rotation offset  $x_c$ , which quantifies the headwind shift between the body and the background flow,

$$x_c = -\frac{h^2}{3\gamma a} \frac{d \ln p_{\text{tot}}}{d \ln a}, \quad (37)$$

where  $p_{\text{tot}} \approx \rho H^2 n^2$  is the total mid-plane pressure and  $dp_{\text{tot}}/dr \sim \rho H^2 n^2/r$  (D. Gangardt et al. 2024). Physically, Keplerian shear together with a nonzero co-rotation offset displaces the hot/under-dense and cold/over-dense lobes asymmetrically. The resulting net thermal torque scales with the ratio  $\lambda/x_c$ .

For embedded objects with accretion luminosity  $L$ , the net thermal torque combines a heating torque (outward, positive) and a cold thermal torque (inward, negative), which is present even for non-luminous bodies. Their sum is written (F. S. Masset 2017b),

$$\Gamma_{\text{therm}} = 1.61 \frac{\gamma - 1}{\gamma} \frac{x_c}{\lambda} \left( \frac{L}{L_c} - 1 \right) \Gamma_0, \quad (38)$$

where  $L$  is the body’s luminosity and

$$L_c = \frac{4\pi G m \rho}{\gamma} \chi \quad (39)$$

is the threshold luminosity where the cold and hot torques cancel.

Equation (38) is appropriate so long as the acoustic timescale is larger than the diffusion timescale within the Bondi radius  $R_B^2/(4\chi) \ll R_B/c_s$ . From this inequality we can define a critical thermal mass (O. M. Guilera et al. 2021),

$$m_c \simeq \frac{c_s \chi}{G}, \quad (40)$$

which corresponds to a dimensionless ratio  $\mu_{\text{th}} \equiv m_c/m$ . From high-resolution simulations, D. A. Velasco Romero & F. S. Masset (2020) found that for  $\mu_{\text{th}} \lesssim 1$ , the embedded object is subjected to a thermal force with a

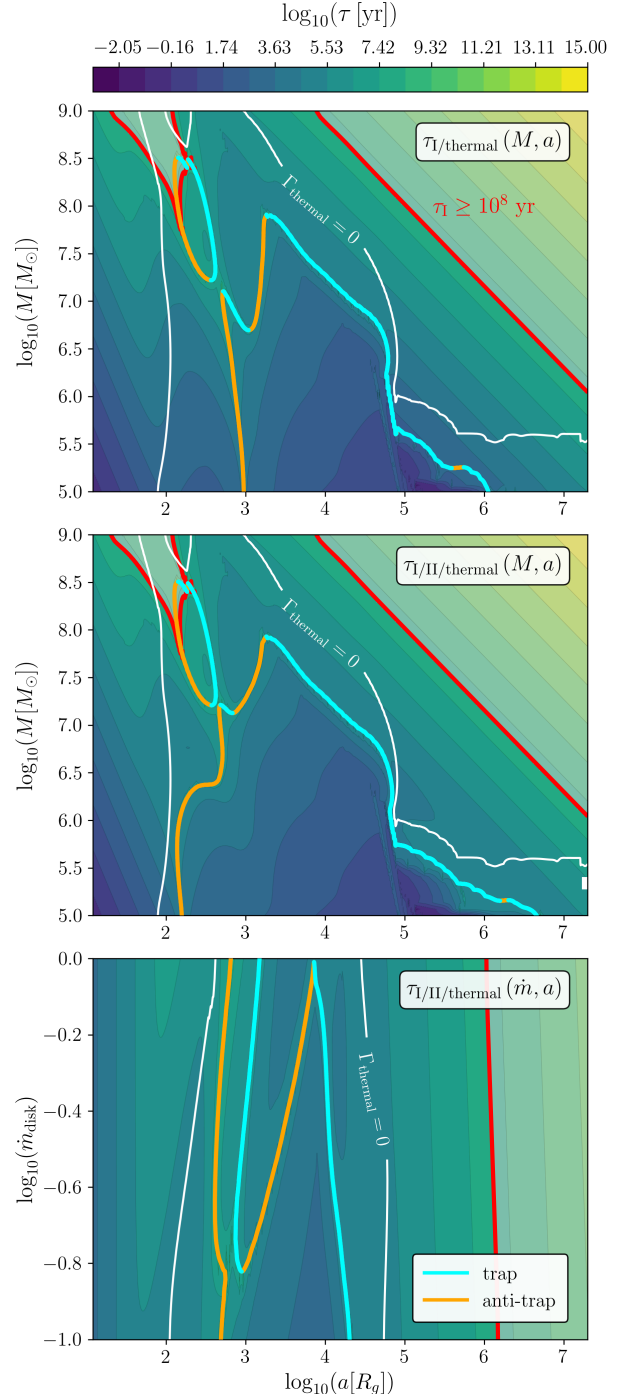


**Figure 3.** Thermal torque migration maps, analogous to Figure 2 but with the additional inclusion of thermal torques (F. S. Masset 2017a). Colored contours show the migration timescale  $\tau$  versus distance from the MBH ( $a[R_g]$ ); the red curve marks  $\tau = 10^8$  yr. As in Figure 2, the top two panels use  $M$  on the y-axis, and the bottom panel uses  $\dot{m}_{\text{disk}}$  (all three panels adopt the same parameters as their Figure 2 counterparts). These maps differ in the torque used to compute  $\tau$ : *Top panel*: we exclude the possibility of gap opening and show  $\tau_{\text{I/thermal}} \propto (\Gamma_{\text{I}} + \Gamma_{\text{GW}} + \Gamma_{\text{thermal}})^{-1}$ , with  $\Gamma_{\text{thermal}}$  given by Equation (41). *Middle and bottom panels*: gap opening is now accounted for and we show  $\tau_{\text{I/II/thermal}} \propto \Gamma_{\text{tot}}^{-1}$ , where  $\Gamma_{\text{tot}} = \Gamma_{\text{I/II}} + \Gamma_{\text{GW}} + \Gamma_{\text{thermal}}$ , and  $\Gamma_{\text{I/II}}$  follows Equation (35). Cyan (orange) lines mark *migration traps (anti-traps)* defined by zero total torque and white contours indicate  $\Gamma_{\text{thermal}} = 0$ .

magnitude in good agreement with the linear theory developed by F. S. Masset (2017b). When  $\mu_{\text{th}} > 1$ , the ratio of the heating torque to its linear estimate decays slowly. D. A. Velasco Romero & F. S. Masset (2020) give an approximate expression that fits the numerical results:

$$\Gamma_{\text{therm}} = \Gamma_{\text{therm,hot}} \frac{4\mu_{\text{th}}}{1 + 4\mu_{\text{th}}} + \Gamma_{\text{therm,cold}} \frac{2\mu_{\text{th}}}{1 + 2\mu_{\text{th}}}, \quad (41)$$

where  $\Gamma_{\text{heat}}$  and  $\Gamma_{\text{cold}}$  refer to the positive and negative terms in Equation (38) respectively.

An additional caveat to the original work of F. S. Masset (2017b) was emphasized by E. Grishin et al. (2024), Equation (38) and 41 assume thermal perturbations are transported by radiative diffusion, an assumption which is only valid when the optical depth over across the diffusion length exceeds unity:  $\tau_\lambda \equiv \lambda/l \gtrsim 1$ , where  $l = (\kappa_e \rho)^{-1}$  is the photon mean free path and  $\kappa_e \simeq 0.34 \text{ cm}^2 \text{ g}^{-1}$  is the electron scattering opacity. Following their implementation, we account for the breakdown toward optically thin conditions with a smooth attenuation factor  $1 - \exp(-\sqrt{\alpha_{\text{disk}}} \tau_\lambda)$ , so that the thermal torque is suppressed when  $\tau_\lambda$  is small.

With this analytical framework in hand, we update the migration timescales in Figure 2 to include the thermal torque. We plot the results in Figure 3. As before, the top and middle panels map the  $(M, a)$  plane, adopting  $m = 10 \text{ M}_\odot$ ,  $\alpha_{\text{disk}} = 0.01$ , and  $\dot{m}_{\text{disk}} = 0.1$ ; the bottom panels presents  $(\dot{m}_{\text{disk}}, a)$  at fixed  $M = 10^7 \text{ M}_\odot$ ,  $\alpha_{\text{disk}} = 0.01$ , and  $m = 10 \text{ M}_\odot$ . Note that we assume the orbiter is accreting at the Eddington rate<sup>7</sup> such that its luminosity is  $L = 4\pi G cm/\kappa_e$ . Contours show the migration timescale  $\tau$ , now computed from the total torque. In the top panel we use  $\tau_{\text{I/thermal}} \propto |\Gamma_{\text{I}} + \Gamma_{\text{thermal}} + \Gamma_{\text{GW}}|^{-1}$ , while in the middle and bottom panels we use  $\tau_{\text{I/II/thermal}} \propto |\Gamma_{\text{I/II}} + \Gamma_{\text{thermal}} + \Gamma_{\text{GW}}|^{-1}$ , where  $\Gamma_{\text{I/II}}$  is the gap-reduced gas torque from Equation (35). Our plots also include a white contour which indicates where  $\Gamma_{\text{thermal}} = 0$ , i.e. where the direction of the torque changes sign.

Our results broadly align with the power-law disk models of E. Grishin et al. (2024). In their framework, positive thermal torques often overwhelm Type I torques

<sup>7</sup> This assumption is motivated by the generally super-Eddington Bondi-Hoyle accretion rates onto embedded BHs (N. C. Stone et al. 2017), which only fall below the Eddington rate for the outer regions of high mass disks, where migration times are usually too long for MMR capture. We thus follow S. Gilbaum & N. C. Stone (2022) in assuming that feedback results in a time-averaged Eddington accretion rate, though we note that this is an uncertain area of accretion physics.

and carve a band of outward migration bounded by a trap and anti-trap. Their trap generally lies between  $10^3$  and  $10^5 R_g$ , shifting inward with increasing  $M$ . They also find that traps disappear at high MBH masses: for  $\dot{m}_{\text{disk}} \sim 0.1$  and 1, traps are confined to  $M \lesssim 10^8$  and  $M \lesssim 10^7 \text{ M}_\odot$  respectively. These results look very similar to the outer migration trap presented in the top panel of Figure 3. However, because E. Grishin et al. (2024) assume a simplified power-law approximation to the E. Sirko & J. Goodman (2003) disk, their model misses a secondary trap near  $a \simeq 10^3 R_g$ , which widens the parameter space for traps up to  $10^{8.5} \text{ M}_\odot$ . This secondary feature is captured in the more detailed disk calculations given by D. Gangardt et al. (2024) and S. Gilbaum et al. (2025). Having used the pAGN of D. Gangardt et al. (2024), our maps track their results.

In the middle panel, migration traps extend to larger radii. This occurs because reducing the effective surface density weakens the Type I torque and allows the thermal term to dominate over an increased range of  $a$ . In the bottom panel, we show changes in the outer and inner traps with  $\dot{m}_{\text{disk}}$ , find that as  $\dot{m}_{\text{disk}}$  increases, the outer trap/anti-trap pair narrows and vanishes for  $M = 10^7 \text{ M}_\odot$  by  $\dot{m}_{\text{disk}} \simeq 1$ , in agreement with E. Grishin et al. (2024). For the same  $M$  the inner trap appears at  $\log_{10}(\dot{m}) \simeq -0.8$  and persists to  $\log_{10}(\dot{m}) \simeq 1$ , remaining near  $a \simeq 10^3 R_g$ .

### 3.2. Eccentricity Damping

In the classic Type-I regime, disk torques also damp the eccentricity of an embedded object. In the linear, small- $e$  limit, H. Tanaka & W. R. Ward (2004) found,

$$\left. \frac{\dot{e}}{e} \right|_{\text{TW04}} \equiv \tau_{e,\text{TW04}}^{-1} \simeq -\frac{3}{4} n \left( \frac{m}{M} \right) \left( \frac{\Sigma a^2}{M} \right) \left( \frac{H}{a} \right)^{-4}. \quad (42)$$

Relative to Type-I migration, this implies  $\tau_{e,\text{TW04}} \sim \tau_{\text{I}} \left( \frac{H}{a} \right)^2$ . In the thin-disk regime relevant here, this makes  $\tau_{e,\text{TW04}}$  several orders of magnitude shorter than the migration timescales shown in Figure 2. These in 3D simulations by P. Cresswell & R. P. Nelson (2008) for small  $e$ , who also showed that once  $e \gtrsim H/a$  the effective damping time increases. As we work in the small- $e$  limit, the H. Tanaka & W. R. Ward (2004) prescription suffices here.

Note that we expect that as in the case of  $\tau_{\text{mig}}$ , the eccentricity damping timescale will lengthen with the local gas density is reduced. By the same reasoning as Equation (35),  $\tau_{e,\text{I/II}} = \Sigma/\Sigma_{\min} \tau_{e,\text{TW04}}$ , maintaining the proportionality constant  $(H/a)^2$  between  $\tau_{\text{I/II}}$  and  $\tau_{e,\text{I/II}}$ .

In §3.1 we noted that heating and cooling also modify migration torques. As shown in O. Chrenko et al.

(2017); H. Eklund & F. S. Masset (2017); S. Fromenteau & F. S. Masset (2019), heating and cooling will likewise alter eccentricity evolution. H. Eklund & F. S. Masset (2017) showed in simulations of luminous, accreting embryos that  $e$  can rise to values comparable to the disk aspect ratio on short timescales. S. Fromenteau & F. S. Masset (2019) extended this with linear theory and provided a small- $e$ , orbit-averaged damping rate

$$\frac{\dot{e}}{e} \simeq \frac{1.46}{t_{\text{thermal}}} \left( \frac{L}{L_c} - 1 \right), \quad (43)$$

where

$$t_{\text{thermal}} = \frac{c_s^2 n \sqrt{\chi/n}}{2(\gamma - 1) G^2 M \rho}, \quad (44)$$

valid for  $ea \ll \lambda$  and  $\lambda \ll H$ . For non-luminous ('cold') bodies with  $L < L_c$ , the linear thermal contribution increases the damping rate relative to the classical isothermal/adiabatic result by roughly a factor of  $\sim H/\lambda$ . For luminous bodies with  $L > L_c$ , the sign in Equation (43) reverses, and the thermal contribution grows the eccentricity. Equation (43) is approximately  $H/\lambda$  times larger than the H. Tanaka & W. R. Ward (2004) damping rate, indicating that thermal torques should nearly always dominate their non-thermal counterparts except where  $L \simeq L_c$  – i.e. the white line shown in Figure 3.

In the luminous case, once  $ea \sim \lambda$ , growth transitions toward a headwind/dynamical friction-like regime and then saturates as the motion becomes transonic. Practically, S. Fromenteau & F. S. Masset (2019) find that the saturation eccentricity lies between  $\lambda/a$  and  $H/a$ .

#### 4. STOCHASTIC FORCES

Dissipative migration of stellar mass objects through the AGN disk will frequently create conditions that appear favorable for resonance capture. However, the dynamically complex environments of AGN create a number of challenges for MMR survivability. In particular, stochastic forcing from (i) gravitational fluctuations driven by turbulence in the disk and (ii) impulsive kicks from stars in the surrounding nuclear cluster can disrupt resonances. The former has been extensively studied in the planetary context (E. T. Johnson et al. 2006; F. C. Adams et al. 2008; H. Rein & J. C. B. Papaloizou 2009; K. Batygin & F. C. Adams 2017); in this section we build on the logic outlined in those works.

In general, acceleration by a perturbative, stochastic force  $\mathbf{F}$  follows a stationary stochastic Gaussian process with an autocorrelation function given by

$$\langle F(t)F(t') \rangle = \langle F^2 \rangle \exp \left( -\frac{|t - t'|}{\tau_c} \right) \quad (45)$$

where  $\tau_c$  is the autocorrelation time. A quantity  $A$  driven by such a force undergoes a random walk, and the

mean square displacement  $\langle \Delta A^2 \rangle$  grows linearly with  $t$  for  $t \gg \tau_c$ . Thus the evolution of  $A$  can be characterized by a constant diffusion coefficient  $\mathcal{D}_A = \langle (\Delta A)^2 \rangle / (2t)$ . H. Rein & J. C. B. Papaloizou (2009) and S. Okuzumi & C. W. Ormel (2013) derived a general set of celestial mechanics equations describing the response of planets to a stochastic force  $\mathbf{F}$ , computing diffusion coefficients in  $a$  and  $e$  according to,

$$\frac{\mathcal{D}_a}{a^2} \propto \mathcal{D}_e \propto \frac{\langle F_\phi^2 \rangle \tau_c}{a^2 n^2}, \quad (46)$$

where  $\mathbf{F} = (F_r, F_\phi)$  has been decomposed into its radial and azimuthal components, whose magnitudes are taken to be comparable.

This general analytic framework can be applied to the specific forcing mechanisms expected in AGN disks, and in the following subsections, we translate  $\langle F_\phi^2 \rangle$  and  $\tau_c$  into quantities appropriate for MRI turbulence and stellar flybys in the nuclear cluster. We calculate diffusion coefficients  $\mathcal{D}_{i,\text{turb}}$  and  $\mathcal{D}_{i,\text{scat}}$ , where  $i$  is a stand-in for the orbital elements  $a$  and  $e$ , and we compare their relative strengths as functions of MBH mass  $M$  and orbital radius  $r$ , as shown in Figure (4).

##### 4.1. Turbulence

MRI turbulence is driven in differentially rotating disks via coupling between the gas and magnetic fields. This interaction excites gas density fluctuations, which give rise to stochastic gravitational forces. From Poisson's equation, a local density perturbation  $\delta\rho$  acting on a characteristic scale  $l$  produces a fluctuating acceleration of order  $4\pi G \delta\rho l$ . In a geometrically thin, MRI-driven disk the characteristic length is of order  $H$  and we can replace fluctuations in  $\delta\rho$  with column density  $\delta\Sigma = 2H\delta\rho$ . Assuming the fractional surface density fluctuations scale as  $\sqrt{\alpha}$ , we can calculate the variance in  $\mathbf{F}$  as

$$\langle F^2 \rangle \sim \alpha \left( \frac{\Sigma a^2}{M} \right)^2 (n^2 a)^2. \quad (47)$$

Under the assumption that the azimuthal and radial components of  $\mathbf{F}$  are comparable, we can write  $\langle F_\phi^2 \rangle \simeq \langle F_r^2 \rangle \simeq \langle F^2 \rangle / 2$ .

Density fluctuations contributing to stochastic forcing lie within  $H$  of the orbiter (J. S. Oishi et al. 2007). Consequently, when the mass of the orbiter is large enough to reduce the local surface density, the stochastic force  $\mathbf{F}$  is also reduced. The lower surface density is parameterized according to Equation (35), where  $\Sigma_{\min}$  denotes the locally depleted, azimuthally averaged surface density within  $\sim H$  of the body due to partial gap-opening by its tidal torques. Accordingly, we replace  $\Sigma$  with

$\Sigma_{\min}$  in Equation (47) when evaluating the diffusion coefficients.

For MRI-driven turbulence,  $\tau_c \sim n^{-1}$  is inferred from simulations (e.g. T. Sano et al. 2004). From Equation (46), the diffusion coefficients are

$$\begin{aligned} \frac{\mathcal{D}_{a,\text{turb}}}{a^2} &\sim 2\mathcal{D}_{e,\text{turb}} \sim \frac{\alpha}{2} \left( \frac{\Sigma_{\min} a^2}{M} \right)^2 n \\ &\simeq \frac{1.8 \times 10^{-8}}{\text{year}} \left( \frac{\alpha}{0.01} \right) \left( \frac{\Sigma_{\min}}{50 \text{ g/cm}^2} \right)^2 \\ &\quad \times \left( \frac{a}{16 \text{ pc}} \right)^{5/2} \left( \frac{M}{10^8 \text{ M}_\odot} \right)^{-3/2}, \end{aligned} \quad (48)$$

where we have incorporated approximate pre-factors from Equation (8) of K. Batygin & F. C. Adams (2017).

#### 4.2. Stellar Flybys

AGN episodes occur when large quantities of interstellar gas flow into a galactic nucleus. Prior to this inflow, most galactic nuclei are populated by an MBH and its surrounding nuclear star cluster (NSC). The quasi-spherical, quasi-isotropic distribution of stars in the NSC creates a population of scatterers that may stochastically influence the orbits of embedded objects migrating in resonance. While strong (large-angle) scatterings are quite rare, the cumulative stochastic forcing from many weak (distant, small-angle) two-body scatterings may in some circumstances force objects out of MMR.

Consider a spherically symmetric nuclear star cluster with a 3D number density profile

$$n_\star(r) = n_{\text{infl}} \left( \frac{a}{a_{\text{infl}}} \right)^{-\gamma}, \quad (49)$$

where we have defined the influence radius to be the radial coordinate enclosing a mass in stars equal to the mass of the MBH. Dynamical modeling of *Hubble Space Telescope* observations of nearby galactic nuclei finds that  $a_{\text{infl}} \approx 16 \text{ pc} (M/10^8 \text{ M}_\odot)^{0.69}$ , with some scatter (N. C. Stone & B. D. Metzger 2016). The stellar density profile is thus normalized by

$$\begin{aligned} n_{\text{infl}} &= \frac{M}{\langle m_\star \rangle} \frac{3 - \gamma}{4\pi a_{\text{infl}}^3} = \\ &\simeq \frac{2.43 \times 10^3}{\text{pc}^3} \left( \frac{3 - \gamma}{1.25} \right) \\ &\quad \times \left( \frac{\langle m_\star \rangle}{\text{M}_\odot} \right)^{-1} \left( \frac{M}{10^8 \text{ M}_\odot} \right)^{-1.07} \end{aligned} \quad (50)$$

where  $\langle m_\star \rangle$  is the mean stellar mass. Assuming a power-law present-day stellar mass function (PDMF)  $dN/dm_\star \propto m_\star^{-\delta_{\text{IMF}}}$  with  $\delta_{\text{IMF}} \in [1.7, 2.35]$  (H. Bartko

et al. 2010; J. R. Lu et al. 2013) and bounds  $m_{\star,\min} = 0.1 \text{ M}_\odot$ ,  $m_{\star,\max} = 120 \text{ M}_\odot$ , the mean stellar mass,  $\langle m_\star \rangle$ , varies between  $0.36 - 1.78 \text{ M}_\odot$ . For simplicity we adopt  $\langle m_\star \rangle = 1 \text{ M}_\odot$ . Additionally, we take  $\gamma = 7/4$ , as is appropriate for a collisionally relaxed single-mass system (J. N. Bahcall & R. A. Wolf 1976), but we also consider  $\gamma = 1$  as an alternate case for an unrelaxed “core” profile, as is prevalent for high-mass MBHs (T. R. Lauer et al. 2005).

The energy relaxation time for a test star embedded in this NSC is, approximately,

$$t_{\text{rel}} = k \frac{\sigma^3(a)}{G^2 n_\star(a) \langle m_\star^2 \rangle \ln \Lambda} \quad (51)$$

where  $\sigma(a) \approx \sqrt{GM/a}/\sqrt{1+\gamma}$  is the (1D) stellar velocity dispersion,  $\langle m_\star^2 \rangle \simeq 23 \text{ M}_\odot^2$  is the second moment of the stellar PDMF<sup>8</sup>,  $\ln \Lambda \approx \ln(0.4M/\langle m_\star \rangle)$  is the Coulomb logarithm, and  $k \approx 0.34$  is a dimensionless number of order unity. This relaxation time can be interpreted in terms of a second-order energy-space diffusion coefficient,  $t_{\text{rel}} = E^2/\mathcal{D}_{E,\text{scat}}$ . For quasi-circular orbits we take  $|E| \simeq GM/(2a)$ , and a change of variables gives

$$\mathcal{D}_{a,\text{scat}} = \left( \frac{da}{dE} \right)^2 \mathcal{D}_{E,\text{scat}} = \frac{a^2}{t_{\text{rel}}}, \quad (52)$$

and from Equation (48), diffusion in eccentricity is related to semi-major axis by

$$\begin{aligned} 2\mathcal{D}_{e,\text{scat}} &\sim \mathcal{D}_{a,\text{scat}}/a^2 \sim t_{\text{rel}}^{-1} \\ &\propto M^{0.69\gamma-2.57} a^{3/2-\gamma} \kappa_\star \langle m_\star \rangle, \end{aligned} \quad (53)$$

where  $\kappa_\star = \langle m_\star^2 \rangle / \langle m_\star \rangle^2$ . For our adopted PDMF,  $\kappa_\star \approx 23$ . For fiducial parameters  $M = 10^8 \text{ M}_\odot$ ,  $a = 16 \text{ pc}$  (i.e.  $a \simeq a_{\text{infl}}$ ),  $\gamma = 7/4$ , and  $\ln \Lambda \simeq 17.5$ , we obtain  $t_{\text{rel}}^{-1} \sim (1.7 \times 10^{10} \text{ yr})^{-1} \simeq 6 \times 10^{-11} \text{ yr}^{-1}$ . Note that for both nuclear cusps  $\gamma = 7/4$  and 1,  $\mathcal{D}_{e,\text{scat}}$  decreases with MBH mass, and decreases (weakly,  $\propto a^{-1/4}$ ) with radius for  $\gamma = 7/4$  while increasing with radius for  $\gamma = 1$ .

#### 4.3. Relative Importance of Turbulence and Stellar Flybys

Having defined two independent sources of stochasticity – MRI turbulence and stellar flybys from the nuclear cluster – it is useful to compare their relative strength across a broader range of AGN-relevant parameters. Diffusion in  $a$  and  $e$  scale identically in the flyby and turbulence contexts,

$$\frac{\mathcal{D}_{a,\text{scat}}}{\mathcal{D}_{a,\text{turb}}} = \frac{\mathcal{D}_{e,\text{scat}}}{\mathcal{D}_{e,\text{turb}}} \simeq \frac{2n^{-1}}{\alpha t_{\text{rel}}} \left( \frac{M}{\Sigma_{\min} a^2} \right)^2. \quad (54)$$

<sup>8</sup> For a power-law  $dN/dm_\star \propto m_\star^{-\delta_{\text{IMF}}}$  with  $m_\star \in [0.1, 120] \text{ M}_\odot$ , choosing  $\delta_{\text{IMF}} \approx 1.88$  yields  $\langle m_\star \rangle \approx 1 \text{ M}_\odot$ ,  $\langle m_\star^2 \rangle \approx 23 \text{ M}_\odot^2$ .

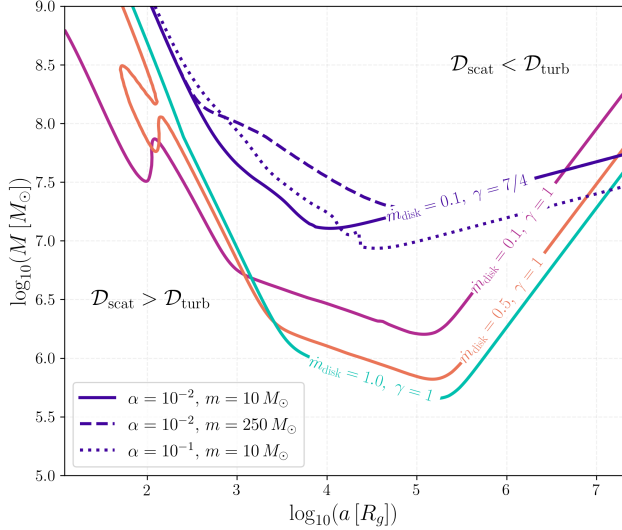


**Figure 4.** Iso-diffusion contours where  $D_{\text{scat}} = D_{\text{turb}}$  in the  $(M/M_{\odot}, a/R_g)$  plane. The dark purple contour shows the fiducial model ( $\alpha = 0.01, m = 10 M_{\odot}, \dot{m}_{\text{disk}} = 0.1, \gamma = 7/4$ ). Dashed and dotted curves vary one disk parameter relative to fiducial: dashed uses  $m = 250 M_{\odot}$ ; dotted uses  $\alpha = 0.1$ . Solid magenta, orange and aquamarine curves adopt a core profile for the NSC stars ( $\gamma = 1$ ) with  $\dot{m}_{\text{disk}} = 0.01, 0.5$  and  $0.1$ , respectively.  $D_{\text{scat}}$  obeys a simple power law with semimajor axis  $a$ , but  $D_{\text{turb}}$  has a more complex evolution driven by the AGN disk model. Scattering achieves greater importance at the smallest and largest radii, where disk turbulence is weakened by declines in  $\Sigma$  arising from radiation pressure dominance and  $Q_T = 1$  self-regulation, respectively.

In Figure 4, we evaluate the relative importance of these distinct processes by plotting the locus  $D_{\text{scat}}/D_{\text{turb}} = 1$ , across the  $(M, a)$  plane for model parameters indicated in the caption.

Global trends in  $M$  and  $a$  space can be identified across all of the curves shown in Figure 4. In the lower left quadrant of the figure (small  $a$  and  $M$ ), stellar scattering is always dominant. This follows from Equation (48),  $\mathcal{D}_{e,\text{turb}} \propto \Sigma_{\min}^2 a^{5/2} M^{-3/2}$ , which scales strongly with  $a$ . Note too that for fixed  $a/R_g$ , decreasing  $M$  strengthens scattering, because  $t_{\text{rel}}$  decreases (smaller  $a_{\text{infl}}$  and larger  $n_{\star}$ ), and in general stellar scattering dominates at low  $M$ .

In addition to the broad trends in  $M$  and  $a$ , the balance between turbulence and scattering is also impacted by model-specific parameters including: the nuclear cusp ( $\gamma$ ), the disk viscosity ( $\alpha$ ), the mass flux through the disk ( $\dot{m}_{\text{disk}}$ ), and the mass of the embedded object ( $m$ ). A steeper cusp (larger  $\gamma$ ) raises the stellar density at small radii, and the relative scattering diffusion rate increases as a result. In Figure 4, the solid purple ( $\gamma = 7/4$ ) and magenta ( $\gamma = 1$ ) curves are differentiated only by their respective  $\gamma$  and illustrate

this dependence clearly – with the scattering-dominant region limited to lower MBH masses in the  $\gamma = 1$  case.

Turbulent diffusion carries an explicit linear dependence on  $\alpha$ , but  $\alpha$  also impacts turbulence implicitly through  $\Sigma$ . For a steady disk, decreasing  $\alpha$  raises  $\Sigma$ , partially offsetting the explicit  $D_{\text{turb}} \propto \alpha$  scaling. To clarify this point it is useful to turn to the scaling relations given in E. Grishin et al. (2024): in the outer, marginally stable disk  $\Sigma \propto \alpha^{-1/3}$ ; deeper in, the inverse scaling steepens to  $\alpha^{-1}$ . This behavior is visible in the dotted dark-purple curve ( $\alpha = 10^{-1}$ ): in the outer disk  $D_{\text{turb}}$  expands relative to the fiducial solid curve ( $\alpha = 10^{-2}$ ), but inside  $10^4 R_g$  the dotted contour lies at or above the solid line.

The disk mass supply rate also influences  $D_{\text{turb}}$  implicitly through  $\Sigma$ . A higher  $\dot{m}_{\text{disk}}$  raises  $\Sigma$  and amplifies turbulent diffusion. This is especially true where Toomre regulation ties  $\Sigma$  closely to the mass supply rate. Note that the magenta, orange and yellow contours in Figure 4 differ only in their  $\dot{m}_{\text{disk}}$ , which are  $0.1, 0.5$ , and  $1.0$  respectively. For  $a > 10^3 R_g$ , increasing  $\dot{m}_{\text{disk}}$  expands the region of parameter space where turbulence dominates scattering.

In Figure 4, the dashed purple line assumes  $m = 250 M_{\odot}$ . This variable enters our diffusion model through  $\Sigma_{\min}$ , the locally depleted surface density near the orbiter. A more massive body opens a deeper partial gap, reducing the disk surface density and hence stochastic gravitational forcing from turbulence. The impact is most evident in the intermediate disk ( $10^3 \leq a/R_g \leq 10^5$ ), where turbulent diffusion would otherwise dominate.

Given that neither stellar scattering or turbulence dominates across all parameter space, it is convenient to combine their effects into a single effective diffusion coefficient. Turbulence and stellar scattering are statistically independent, sourced by different components (gas vs. stars). Here we propose a conservative effective diffusion  $\mathcal{D}_{\text{eff}}$ , adding the turbulent and scattering coefficients in quadrature. In the remainder of this paper, we therefore use

$$\frac{\mathcal{D}_{a,\text{eff}}}{a^2} \sim 2\mathcal{D}_{e,\text{eff}} \sim 2\sqrt{\mathcal{D}_{e,\text{turb}}^2 + \mathcal{D}_{e,\text{scat}}^2}. \quad (55)$$

to evaluate the stability of MMR resonances to stochastic forcing. We illustrate the effective eccentricity-diffusion timescales in Figure 5 for fiducial disk parameters ( $\alpha = 0.01, \dot{m}_{\text{disk}} = 0.1$ ) and an embedded mass  $m = 10 M_{\odot}$ . The top panel adopts a nuclear cusp slope  $\gamma = 7/4$ , and the bottom panel  $\gamma = 1$ . Cyan (top) and white (bottom) curves mark where scattering and turbulence contribute equally,  $D_{\text{scat}} = D_{\text{turb}}$ , corresponding to the solid purple and magenta contours in

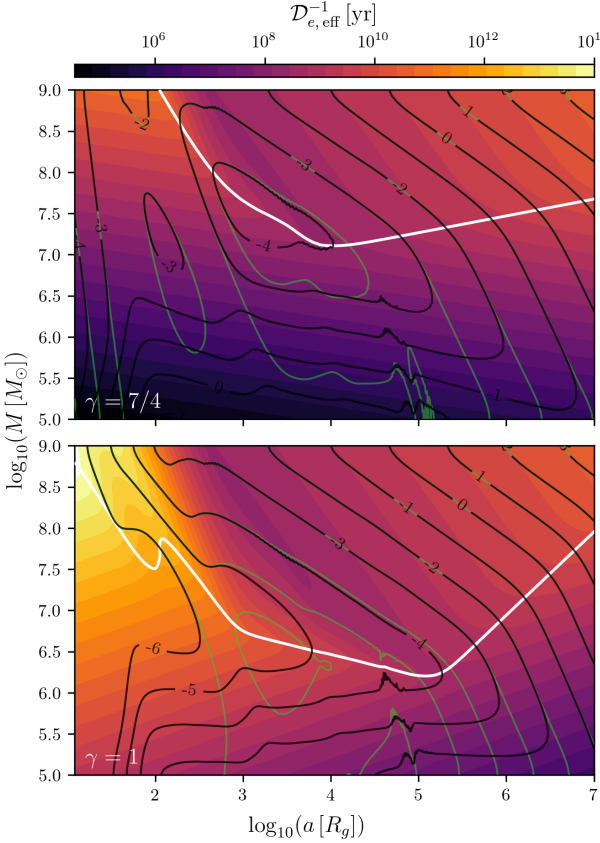


**Figure 5.** Inverse effective diffusion,  $D_{e,\text{eff}}^{-1}$ , across the  $(\log_{10}(M [M_\odot]), \log_{10}(a [R_g]))$  plane. Filled contours show  $D_{e,\text{eff}}^{-1}$  [yr] computed from turbulent and scattering contributions added in quadrature. white contours indicates where  $D_{e,\text{scat}} = D_{e,\text{turb}}$ . *Top:* scattering term evaluated for a stellar cusp with slope  $\gamma = 7/4$ . Black contours show where the product of migration timescale and diffusion,  $\tau_{\text{I/II}} D_{e,\text{eff}} = 10^x$  and contour labels show  $x \in [-4, 3]$ . Green contours assume only Type-I migration *Bottom:*  $\gamma = 1$  and  $x \in [-6, 3]$ .

Figure 4. In the  $\gamma = 7/4$  case, diffusion is strongest at low  $a$  and  $M$ , generally weakening toward larger radii and higher MBH masses, with a distinct island of enhanced diffusion at intermediate radii ( $\sim 10^3$ – $10^4$ ,  $R_g$ ) and high  $M$ . A similar island appears for  $\gamma = 1$ , though the overall peak shifts toward smaller  $M$  and larger  $a$ . Black contours show the dimensionless product of migration time and diffusion,  $\tau_{\text{I/II}} D_{e,\text{eff}} = 10^x$ , with labels indicating  $x = \log_{10}(\tau_{\text{I/II}} D_{e,\text{eff}})$ . Green contours display the same criterion but computed under pure Type-I migration (no gap opening). The interplay between migration and diffusion implied by these contours is examined in the next section.

## 5. CRITERION FOR RESONANCE DISRUPTION

With analytic representations of an embedded object’s interactions with other bodies in the disk (§2), the MBH (§2.1), the nuclear star cluster (§4.2), and the disk itself (§3 and §4.1), we are now positioned to evaluate the stability of MMRs in AGN.

Following K. Batygin & F. C. Adams (2017), we track the evolution of the resonant offset  $\xi \equiv n_2/n_1 - (k+1)/k$  and the eccentricity vector amplitude  $\sigma_c$ , which together quantify the system’s distance from exact resonance. We model their evolution as a competition between turbulent forcing and disk-driven damping, yielding an analytically tractable Ornstein-Uhlenbeck (OU) process for the evolving variable  $X_t \in \{\xi, \sigma_c\}$ ,

$$dX_t = -\kappa X_t dt + \sigma dW_t, \quad (56)$$

where  $\kappa$  is the linear damping rate toward  $X = 0$ ,  $\sigma$  sets the strength of the stochastic forcing, and  $W_t$  is a Wiener process. As  $t \rightarrow \infty$ ,  $X_t$  approaches a stationary Gaussian with variance  $\sigma^2/(2\kappa)$ . Comparing the steady-state rms,  $\langle X^2 \rangle^{1/2} = \sigma/\sqrt{2\kappa}$ , to the intrinsic resonance half-width  $\Delta X_{\text{res}}$  provides a quantitative disruption criterion: resonance breaks when  $\langle X^2 \rangle^{1/2} \gtrsim \Delta X_{\text{res}}$ .

### 5.1. Diffusion of Semi-major Axes

Diffusion in  $\xi$  inherits from diffusion in  $(a_1, a_2)$  via the multivariate Itô chain rule. Assuming that the semi-major axes execute independent Gaussian diffusion with a common coefficient  $D_{a,\text{eff}}$ , diffusion in  $\xi$  is given by

$$\begin{aligned} D_\xi &= D_{a,\text{eff}} \left[ \left( \frac{\partial \xi}{\partial a_1} \right)^2 + \left( \frac{\partial \xi}{\partial a_2} \right)^2 \right] \\ &\simeq \left( \frac{3}{2} \right)^2 \frac{2 D_{a,\text{eff}}}{\langle a \rangle^2}, \end{aligned} \quad (57)$$

where in the second line of Equation (57), we invoke the compact limit,  $a_1 \approx a_2 \approx \langle a \rangle$ .

Disk-driven damping of  $\xi$  follows from

$$\frac{d\xi}{dt} \simeq \frac{3\xi}{2} \left( \frac{\dot{a}_1}{a_1} - \frac{\dot{a}_2}{a_2} \right) = -\frac{3\xi}{2} \tau_{\text{rel}}^{-1}, \quad (58)$$

where we define migration timescales  $\tau_i \equiv a_i/\dot{a}_i$  and  $\tau_{\text{rel}}^{-1} \equiv \tau_2^{-1} - \tau_1^{-1}$ . For fixed disk conditions and comparable  $m_1, m_2$ ,  $\tau_{\text{rel}} \propto |m_1 - m_2|$ , implying an upper bound  $\tau_{\text{rel}} \lesssim \tau_{\text{mig}}(m_1 + m_2)$ . In what follows we adopt the conservative replacement  $\tau_{\text{rel}} \rightarrow \tau_{\text{mig}}(m_1 + m_2)$ , thereby maximizing drift in  $\xi$ .

Combining Equations 57 and 58 yields an OU stochastic differential equation

$$d\xi = \frac{3}{2} \sqrt{\frac{2 D_{a,\text{eff}}}{\langle a \rangle^2}} dW_t - \frac{3}{2} \frac{\xi}{\tau_{\text{mig}}} dt, \quad (59)$$

so that the steady-state rms is

$$\delta\xi = \sqrt{\frac{3}{2} \frac{\mathcal{D}_{a,\text{eff}} \tau_{\text{mig}}}{\langle a \rangle^2}}. \quad (60)$$

The resonant bandwidth  $\Delta\xi$ , is maximized at the onset of libration (i.e. when the resonance first appears at  $\delta = 0$ ) and is given by (K. Batygin 2015)

$$\Delta\xi \simeq 5 \left[ \frac{\sqrt{k} (m_1 + m_2)}{M} \right]^{2/3}. \quad (61)$$

Here  $\Delta\xi$  is the offset required to cross the separatrix, whereas  $\delta\xi$  is a measure of the width of the distribution in  $\xi$  under stochastic evolution. As argued in K. Batygin & F. C. Adams (2017), disruption of the resonance occurs when the ratio of these quantities exceeds unity

$$\frac{\delta\xi}{\Delta\xi} \simeq 1.9 \times 10^3 \sqrt{\left( \frac{\mathcal{D}_{a,\text{eff}} \tau_{\text{mig}}}{\langle a \rangle^2} \right)} \left( \frac{k}{2} \right)^{-1/3} \times \left( \frac{M}{10^7 M_\odot} \right)^{2/3} \left( \frac{m_1 + m_2}{10 M_\odot} \right)^{-2/3} \gtrsim 1. \quad (62)$$

In practice, it is convenient to track the related diagnostic  $\tau_{\text{mig}} \mathcal{D}_{e,\text{eff}} \sim 10^x$ : resonance breaking is expected near  $x \sim 10^{-6} (q/10^6)^{-2/3}$ , where  $q \equiv (m_1 + m_2)/M$ . Turning to Figure 5, for  $m_1 + m_2 \simeq 10 M_\odot$  and  $M \simeq 10^7 M_\odot$  we find  $\mathcal{D}_{e,\text{eff}}^{-1}$  large enough (and  $\tau_{\text{mig}}$  short enough) to approach  $x \sim 10^{-6}$  only for  $\gamma = 1$  and  $a \lesssim 10^3 R_g$ , assuming a Type-I/II torque prescription.

We explicitly illustrate the resonance breaking criterion in Figure 6, plotting the locus  $\delta\chi = \Delta\chi$  in the  $(\log_{10} M, \log_{10} a)$  plane for  $k = 2$ . Regions shaded gray (above and to the right of the curves) are expected to undergo stochastic resonance breaking, while those below are stable. The top row compares Type-I (left) to Type-I/II (right) migration prescriptions; line colors encode either the total embedded mass (top row) or the Eddington ratio (bottom row), while solid vs. dashed styles denote  $\gamma = 1$  vs.  $\gamma = 7/4$ . Red curves overplot the independent condition for secular GR-induced disruption; where these lie below the stochastic boundary, GR precession alone is sufficient to unbind the resonance.

Broadly, in regions where turbulent forcing dominates – typically at larger  $a \gtrsim 10^3 R_g$  and toward higher  $M$  – the effective diffusion rate  $\mathcal{D}_{e,\text{eff}}$  is large relative to  $\tau_{\text{mig}}$  and resonances are more fragile. Steeper cusps ( $\gamma = 7/4$ ) further shrink the stable region, particularly between  $a \sim 10^{2-4} R_g$  where diffusion timescales are minimized and  $\tau_{\text{mig}}$  is relatively large. At the smallest radii, GW-driven migration can re-stabilize resonances,

but in this inner zone secular GR forcing itself typically destabilizes them.

When we include gap opening, the region of parameter space that supports stable resonances contracts markedly. This is most evident at low MBH mass  $M$ , where the gap-opening parameter  $K \propto (m/M)^2$  is large and the surface density is depleted around the embedded mass. Increasing the AGN Eddington ratio  $\dot{m}_{\text{disk}}$  partly offsets this by raising  $\Sigma$  and the scale height  $H$ , thereby reducing  $K$ . When we include Type-II torques and neglect thermal torques, we therefore expect MMRs to largely disappear, surviving only in small islands at intermediate radii and for sufficiently large embedded masses.

In Figure 7 we recompute  $\tau_{\text{mig}}$  including thermal torques. The layout mirrors Figure 6: the top row varies the total embedded mass, the bottom row varies the disk mass flux, and we compare Type-I (left) to Type-I/II (right) prescriptions for angular-momentum exchange. To isolate the maximal stability case, we show only the  $\gamma = 1$  cusp (solid lines). Dotted curves mark the location of traps/anti-traps where  $\tau_{\text{mig}} \rightarrow \infty$ . Recall that our disruption criterion depends on the magnitude of the migration timescale and is agnostic to the torque sign. Notably, in the Type-II regime at low  $M$ , the inclusion of thermal torques stabilizes resonances interior to the migration trap, where the hot (outward) thermal torque dominates. We conclude that, so long as a migrator is sufficiently luminous, resonance locking can remain robust in this band.

At migration traps (or anti-traps) the net torque is  $\Gamma_{\text{tot}}(a) = 0$ , so a single body has  $\dot{a} = 0$  and hence  $\tau_{\text{mig}} \rightarrow \infty$ , implying resonance breaking. However, our disruption criterion used  $\tau_{\text{mig}}$  as a convenient proxy for the *relative* migration timescale, which is overly conservative near traps. Unless both bodies sit exactly at the same zero-torque radius, their torques differ slightly and  $\tau_{\text{rel}}$  will be finite.  $\tau_{\text{rel}}$  is set by the local slope  $\partial\Gamma/\partial a$  and the pair's separation across the trap. Consequently, where trap/anti-trap curves intersect regions of widespread resonant stability – where diffusion is modest and migration is fast – long-lived resonant locking will persist, even though the single-body  $\tau_{\text{mig}}$  formally diverges at the trap center.

Note that our treatment emphasizes an absolute disruption criterion. However, in regions of parameter space where resonance breaking is predicted, the OU process reduces – to first order – to pure diffusion in  $\xi$ . A simple break-time estimate then follows by setting the rms equal to the resonant bandwidth,  $\sqrt{2\mathcal{D}_\xi t_{\text{break}}} =$

$\Delta\xi$ , yielding

$$\begin{aligned} t_{\text{break}} &\simeq \frac{(\Delta\xi)^2}{2\mathcal{D}_\xi} \\ &\simeq 92 \text{ yr} \left(\frac{k}{2}\right)^{2/3} \left(\frac{m_1 + m_2}{10 M_\odot}\right)^{4/3} \\ &\quad \times \left(\frac{M}{10^8 M_\odot}\right)^{-4/3} \left(\frac{\mathcal{D}_\xi}{10^{-10} \text{ yr}^{-1}}\right)^{-1}. \end{aligned} \quad (63)$$

Once a migrator stochastically exists one resonance it may drift and subsequently be captured into another resonance of a higher harmonic  $k$  or altogether different order. Thus while individual resonances may break, the time-averaged probability of being in *some resonance* over the disk lifetime can remain substantial. Quantifying this occupancy – and its implications for merger rates – will be the subject of future work.

## 5.2. Diffusion in eccentricity

Again following K. Batygin & F. C. Adams (2017), to obtain an estimate for diffusion in eccentricity it is convenient to use the Hamiltonian variable  $\tilde{\Psi}$ , which is directly proportional to the generalized combined eccentricity variable  $\sigma_c$ . If the two components of the combined eccentricity vector experience diffusion with coefficient  $\mathcal{D}_{e,\text{eff}}$ , then the combined diffusion amplitude is  $\mathcal{D}_{\sigma_c} = \sqrt{2}\mathcal{D}_{e,\text{eff}}$ , so the stationary dispersion  $\sigma_c$  is

$$\delta\sigma_c \simeq \sqrt{\mathcal{D}_{\sigma_c} \tau_e} \quad (64)$$

where  $\tau_e$  is the eccentricity damping timescale defined in §3.2. At resonance inception the half-width in  $\tilde{\Psi}$  is  $\Delta\tilde{\Psi}/2 = 2$  (K. Batygin 2015) which is equivalent to the half-width in the eccentricity variable  $\Delta\sigma_c = 2$ . Combining these, we obtain a second criterion for resonance disruption, this time in eccentricity

$$\frac{\delta\sigma_c}{\Delta\sigma_c} \simeq \frac{\sqrt{\mathcal{D}_{\sigma_c} \tau_e}}{2} \gtrsim 1. \quad (65)$$

Up to order-unity factors, one finds  $\mathcal{D}_{\sigma_c} \sim \mathcal{D}_\xi$ . If  $\tau_e$  follows the classic H. Tanaka & W. R. Ward (2004) scaling (Equation 42), then typically  $\tau_{e,\text{TW04}} \ll \tau_{I/II}$  and hence  $\delta\sigma_c \ll \delta\xi$ . Moreover, for reasonable parameters we also have  $\Delta\xi \ll \Delta\sigma_c$ . Together these imply that resonance breaking proceeds far more rapidly in the  $\xi$  channel than through eccentricity.

Including thermal effects does not qualitatively change this conclusion. Where cold thermal torques dominate, eccentricity damping is strengthened and resonances are more robust to diffusion. Where hot thermal torques dominate, eccentricity can grow toward the disk aspect ratio,  $e \sim H/a$  (H. Eklund & F. S. Masset 2017;

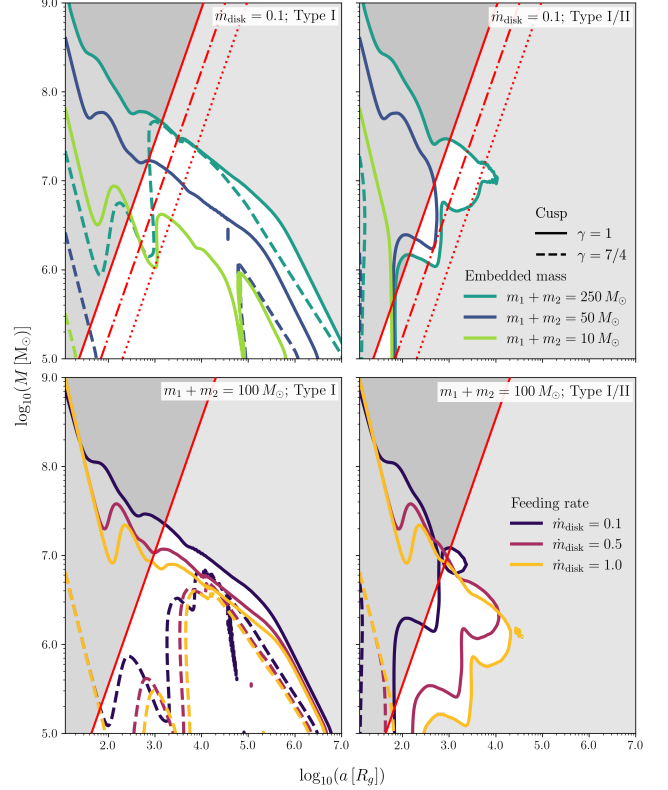


**Figure 6.** Contours indicate where the resonance destabilization condition  $\delta\chi = \Delta\chi$  is met in the  $(\log_{10}(M/M_\odot), \log_{10}(a/R_g))$  plane. Gray shading above and to the right the contours indicates regions where MMRs are expected to break due to stochastic forcing. Overplotted in red are loci where deterministic GR forcing from apsidal precession is expected to break resonances. All curves assume  $k = 2$ .

*Top-left:* Eddington ratio  $\dot{m}_{\text{disk}} = 0.1$  [ $M_{\text{Edd}}$ ]. Colors denote the summed embedded object masses: aquamarine -  $250 M_\odot$ ; dark blue -  $50 M_\odot$ ; green -  $10 M_\odot$ . Solid curves assume a nuclear stellar cusp with slow  $\gamma = 1$ ; dashed curves show  $\gamma = 7/4$ . The solid red line corresponds to GR induced resonance breaking for the largest embedded mass ( $250 M_\odot$ ), the dash-dotted line to  $50 M_\odot$ , and the dotted line to  $10 M_\odot$ .

*Top-right:* Same color/line scheme as top-left, but migration rates assume Type-I/II prescription.

*Bottom-left and right:* Fixed embedded-object mass  $m = 100 M_\odot$ . Colors now indicate the disk mass flux in Eddington units: dark purple -  $\dot{m}_{\text{disk}} = 0.1$ ; magenta -  $\dot{m}_{\text{disk}} = 0.5$ ; orange -  $\dot{m}_{\text{disk}} = 1.0$ . Solid vs dashed lines retain the  $\gamma = 1$  vs.  $\gamma = 7/4$  convention. The solid red line still indicates where GR forces dominate resonant coupling, but is now set according to the fixed mass  $m_1 + m_2 = 100 M_\odot$ .

S. Fromenteau & F. S. Masset 2019). Even adopting  $\delta\sigma_c \sim H/a$  as a conservative ceiling, a geometrically thin disk still satisfies  $\delta\sigma_c \ll \Delta\sigma_c$ , so the eccentricity-based breaking criterion is not met. Thus, in practice, stochastic disruption is controlled primarily by diffusion in  $\xi$ , with eccentricity diffusion playing a secondary role.

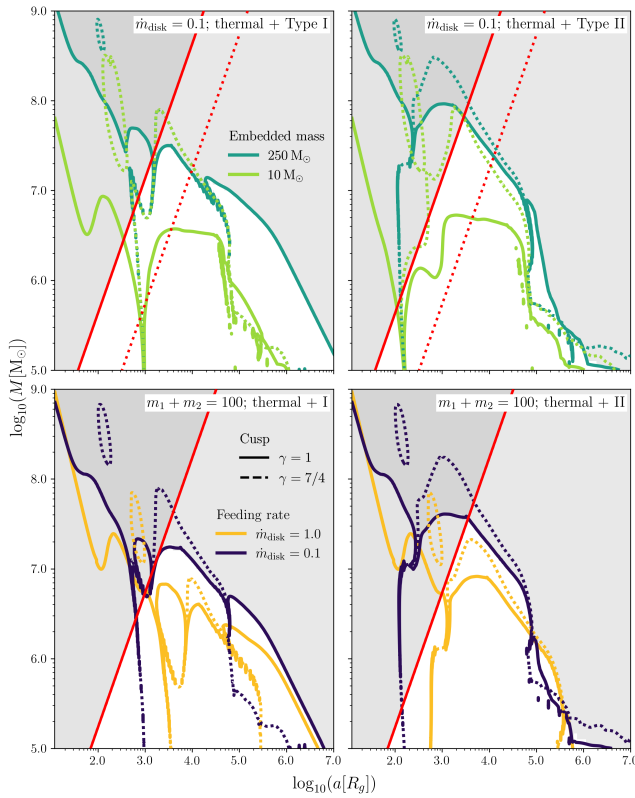


**Figure 7.** Contours where  $\delta\chi = \Delta\chi$  in the  $(\log_{10}(M [\mathrm{M}_\odot]), \log_{10}(a [R_g]))$  plane, now including thermal torques in the migration prescription. As before, gray shading above the contour denotes regions where MMRs are expected to break. All panels assume  $k = 2$  and a core cusp  $\gamma = 1$  (maximum resonance survival). All resonance breaking contours are shown as solid lines. Dotted curves indicate the locations of thermal migration traps/anti-traps.

*Left column:* Thermal + Type-I migration.

*Right column:* Thermal + Type-I/II migration.

*Top row (varying embedded mass):* Colors denote total embedded mass; aquamarine –  $250 \mathrm{M}_\odot$  and green –  $10 \mathrm{M}_\odot$ . Over plotted in red are GR resonance-breaking loci: solid red for  $250 \mathrm{M}_\odot$  and dotted for  $10 \mathrm{M}_\odot$ .

*Bottom row (varying the Eddington ratio):* Colors denote  $\dot{m}_{\mathrm{disk}}$ ; purple –  $\dot{m}_{\mathrm{disk}} = 1.0$  and yellow –  $\dot{m}_{\mathrm{disk}} = 0.1$  in Eddington units.

## 6. DISCUSSION

Do MMRs exist for embedded stellar mass objects in AGN disks? Yes, sometimes. Are MMRs common? The answer to this question is more nuanced, and ultimately model-dependent, as we have seen in Figures 6 and 7. If we neglect the role of thermal torques (Figure 6), then MMRs are quite rare, and exist only over quite narrow radial ranges for AGN in the mass window  $10^5 \lesssim M/M_\odot \lesssim 10^7$ . But if we consider thermal torques (Figure 7), then the picture for MMR survival becomes more favorable, and MMRs may persist over 1-3 orders

of magnitude in radius  $a/R_g$  within the same mass window ( $10^5 \lesssim M/M_\odot \lesssim 10^7$ ). Because the thermal torque depends on uncertain details of accretion feedback into AGN disks, we have considered the durability of resonances with and without it (and will discuss this further in §6.2).

Why does it matter whether or not MMRs are stable in AGN? Stars and stellar mass BHs in AGN generally experience differential migration, and will frequently overtake one another when moving through the AGN disk. *Convergent* differential migration will thus often create the conditions for resonance capture, and if an  $\mathcal{O}(1)$  fraction of migrating BHs do indeed capture into MMRs, the implications for GW production in AGN will be significant. As an extreme case, we can imagine a scenario where all migrating BHs capture into resonant chains or convoys, and where migration traps are wholly absent from AGN. In this situation, it would become *impossible* for AGN to synthesize new binary BH systems out of individual embedded BHs. As binary assembly from single-single capture (mediated by either gas dynamical friction or minidisk interactions during close flybys) has the greatest potential for producing a large population of binary BHs in AGN, this scenario would greatly reduce the maximum LVK-band merger rate from the AGN channel.<sup>9</sup> Moreover, stable MMR capture would completely foreclose the possibility of repeated mergers and hierarchical growth of BHs up to e.g. characteristic masses forbidden by single-star evolution, which today is viewed as one of the most promising “smoking guns” of the AGN channel. This would also alter the mass function of wet EMRIs visible in the *LISA* band relative to the situation if MMRs are rare (Z. Pan et al. 2022).

In the previous sections, however, we have seen that mean motion resonances in AGN disks are generally fragile. In particular, leading-order post-Newtonian precession will overwhelm apsidal libration and destroy MMRs at sufficiently small radii  $a$  (Figure 1). MMRs can persist down to smaller dimensionless radii  $a/R_g$  for less extreme mass ratios  $q = m/M_{\mathrm{BH}}$ , favoring resonance survival for (i) IMBH primaries and (ii) relatively large stellar mass BHs<sup>10</sup>. Ultimately, any MBH-BH combination will only be capable of producing stable

<sup>9</sup> This “worst case” scenario would not completely deactivate the AGN channel for LVK-band mergers, as binary BHs could still be captured from a pre-existing NSC population or formed *in situ* Toomre instability.

<sup>10</sup> This factor is noteworthy given the recent LVK observations of  $m \sim 100 M_\odot$  BHs in the pair instability mass gap forbidden to single star evolution. Such BHs are likely the product of repeated mergers and hierarchical growth, which may only be

resonances outside of a critical radius

$$R_{\text{GR}} = \frac{2}{(3f_{k+1,27})^{1/3}} \frac{k^{8/9}}{(k+1)^{14/9}} \left( 1 - \left( \frac{k+1}{k} \right)^{-5/3} \right) \times R_g \left( \frac{M}{m_1 + m_2} \right)^{2/3} \quad (66)$$

If we imagine a stable pair of binary BHs migrating inwards in resonance with each other, the MMR will break once they reach  $R \approx R_{\text{GR}}$ . Interestingly, however,  $R_{\text{GR}}$  is a decreasing function of the MMR harmonic  $k$  (as what ultimately matters is not the single-body apsidal precession rate  $\dot{\omega}_{\text{GR}}$  but rather the differential apsidal precession rate  $\Delta\dot{\omega}_{\text{GR}}$ ), so if the migration is still convergent at  $R_{\text{GR}}$ , the two objects may cascade through a sequence of MMRs with increasingly high harmonic numbers  $k$ .

While deterministic precession always eliminates MMRs at  $a < R_{\text{GR}}$ , stochastic forcing will sometimes, though not always, have the same effect at larger radii. We have seen that stochastic perturbations are most destabilizing to MMRs around larger MBHs. For the largest MBHs, disk turbulence is the dominant form of stochastic perturbation, while for the smallest MBHs, it is instead stellar scattering that dominates. The transition between these two types of perturbations is radius-dependent, and further depends on AGN parameters (see Figure 4), but in the radii of greatest interest, the transition from scattering-dominated to turbulence-dominated stochasticity occurs for  $M/M_{\odot} \sim 10^{6-7.5}$ .

Accounting for both deterministic (Figure 1) and stochastic (Figure 6) destabilization of MMRs, we see that MMRs are generally fragile in most AGN. For low-mass migrators ( $m \sim 1M_{\odot}$ ), MMRs will rarely be stable in any AGN disks. Higher mass migrators ( $m \sim 100M_{\odot}$ ) are more robust against GR precession and disk turbulence. As mentioned previously, MMRs only exist in a narrow radial range if thermal torques are neglected. In the case when thermal torques do exist and are described by standard formulae (F. S. Masset 2017b), we can identify three distinct AGN regimes:

1. High mass AGN ( $M \gtrsim 10^{7.5}M_{\odot}$ ): stable MMRs never exist.
2. Low mass AGN ( $M \lesssim 10^{6.5}M_{\odot}$ ): stable MMRs always exist. They are generally destabilized by stellar scatterings for  $a \gtrsim 10^{5-6}R_g$  and by GR precession for  $a \lesssim 10^{2-3}R_g$ ; stochastic effects may sometimes play a destabilizing role in the  $a \sim 10^{2-3}R_g$

possible in AGN disks due to the challenge that GW recoil kicks pose for merger product retention.

range as well. Regions of MMR stability are generally interior to a migration trap and exterior to an anti-trap.

3. Intermediate mass AGN ( $10^{6.5} \lesssim M/M_{\odot} \lesssim 10^{7.5}$ ): in this regime MMRs may or may not be stable depending on system parameters; generally, MMR stability is favored by lower  $M$ , lower  $\dot{m}_{\text{disk}}$ , and higher  $m$  values. As with the high mass case, radial zones of MMR stability are generally in between a trap and an anti-trap (i.e. they are regions of outward migration).

There are several observable implications of this varied MMR landscape. First, we can say that in high mass AGN, convergent migration will efficiently form LVK-band BH-BH binaries, as MMRs are too unstable to prevent this from occurring. In low and intermediate mass AGN, MMRs will be common in the zone of outward migration that lies between an inner anti-trap and an exterior trap produced by thermal torques. Whether this affects LVK production rates will depend on the radial origin of most single BHs embedded in AGN disks. If the majority of such BHs are formed *in situ* via Toomre fragmentation, it will usually be at larger radii, from which they can migrate inwards towards migration traps. Across much of the MBH parameter space, traps lie along or exterior to MMR stability bounds, leading to pile-ups and enhanced likelihood for mergers. Narrow MBH windows exist (just below and above  $10^6 M_{\odot}$ ) where a stable-MMR swath lies exterior to the trap, so resonant capture could delay or suppress mergers. For sufficiently massive embedded objects, gap opening can lower local opacity and thereby weaken thermal torques; such BHs experience Type-II migration only, and pass through the trap. We return to these caveats in §6.2.

BHs and other stellar mass objects may originate in the inner disk if they are captured by gas drag from pre-existing NSC populations. While retrograde captures will be quickly excited to high eccentricity and lost from the AGN disk (A. Generozov & H. B. Perets 2023), prograde captures will circularize. Realistic  $\Sigma(r)$  profiles imply that capture rates will fall off as functions of radius, so that a large fraction of gas-captured BHs may originate in the region of outward migration (where MMRs are most likely to be stable). It is only for this subset of disk-embedded BHs that stable resonant chains can reduce orbit crossings and LVK binary formation rates. Given the complexity of modeling the joint evolution of AGN disks and their embedded BH populations (M. Epstein-Martin et al. 2025), we do not attempt in this paper to determine the overall impact of

MMRs on LVK-band merger rates, but note here that we have isolated the particular  $M$  and  $a/R_g$  values where they *can* matter.

Because MMR stability appears co-extensive with regions of outward migration due to thermal torques, MMRs appear unlikely to have a major impact on wet EMRI rates and properties. The no-MMR regime of high mass AGN is not relevant for wet EMRIs, as  $M \gtrsim 10^{7.5} M_\odot$  lies well outside the *LISA* band. For low and intermediate mass AGN whose EMRIs will be detectable, MMRs could in principle affect EMRI properties (if e.g. they were ubiquitous enough to prevent hierarchical mergers from repeated binary formation) but this appears not to be the case.

The previous three paragraphs have worked under the assumption that thermal torques exist and can be described by standard formulae from the protoplanetary literature. These formulae rely on a hierarchy of distance scales,  $x_c < \lambda < H$ , as well as the broader assumption that heating from the embedded object only creates a linear perturbation in the disk structure (i.e.  $L_{\text{Edd}}(m)/H^2 < \sigma T_{\text{eff}}^4$ , assuming that the accretion luminosity of the embedded object is Eddington limited). Both the linear perturbation assumption and the  $\lambda < H$  assumption will break down at the largest radii (E. Grishin et al. 2024). Linearity of the heating perturbation becomes more challenging to maintain for smaller  $M$  values ( $M \lesssim 10^7$ ). If thermal torques are dramatically weakened in these regimes and the situation becomes more Type I-like, then MMRs will be even less robust.

### 6.1. Imprints on Gravitational Waveforms

If high- $k$  MMRs can survive down to  $\sim 10-100 R_g$ , an EMRI's waveform could be sensitive to the accompanying perturbations. *LISA* will track up to  $\sim 10^5$  orbital cycles (P. Amaro-Seoane et al. 2023), making even weak environmental forces measurable. Prior work has shown that gas torques (Type-I/II), accretion drag, galactic potentials, light scalar fields, and tidal resonances can all imprint detectable phase shifts (e.g., B. Kocsis et al. 2011; N. Yunes et al. 2011; P. Amaro-Seoane et al. 2012; H. Yang & M. Casals 2017; B. Bonga et al. 2019; V. Cardoso et al. 2022; S. Barsanti et al. 2023). A long-lived high- $k$  resonant companion would impart quasi-periodic torques leading to cumulative phase drift that could, in principle, be identified with *LISA*.

For stellar mass binaries in the LVK band, maintaining resonance to  $\sim 10-100 R_g$  would enable single-single capture and merger deep in the SMBH potential, where strong-field effects are unavoidable. The center-of-mass acceleration induces time-varying Doppler shifts and gravitational redshift (K. Inayoshi et al. 2017). Close

alignment can yield GW ‘echoes’ (a secondary, delayed copy of the signal) and strong lensing effects (Y. Meiron et al. 2017; L. Gondán & B. Kocsis 2022; W.-L. Xu et al. 2025). Although a resonant cascade to high- $k$  harmonics is for now speculative, and could be derailed by (e.g.) higher order post-Newtonian terms or high- $k$  resonance overlap, the prospect of strong-field signatures for both LVK and *LISA*-band GWs merits further investigation.

### 6.2. Caveats and Future Work

As noted in §3, there is not yet consensus on the most appropriate AGN disk model – especially in the outer disk, where the high mass flux needed to power an AGN drives the disk toward self-gravitating collapse. In the class of models most commonly used to describe AGN structure, this tendency is explicitly countered by self-regulating star-formation feedback. We use the E. Sirko & J. Goodman (2003) framework because it provides a clear parameterization of steady-state disk properties with a radially constant  $\dot{m}_{\text{disk}}$ , isolating the impact of the disk mass flux. This choice is, however, somewhat less physically motivated than the common alternative, proposed by T. A. Thompson et al. (2005), which includes star-formation driven gas consumption, and decreasing  $\dot{m}_{\text{disk}}$  nearer to the MBH. The decrease in  $\dot{m}_{\text{disk}}$  across the Thompson-type disk maps to a lower surface density  $\Sigma$ , thereby reducing turbulent diffusion and potentially enlarging regions where MMRs can survive – highlighted in Figure 6 and Figure 7.

Alternative sources of disk-stabilizing pressure support have also been proposed: both magnetic pressure (P. F. Hopkins et al. 2024; H. J. Gerling-Dunsmore et al. 2025) and accretion onto embedded stellar-mass BHs (Y. Levin 2003, 2007) have been shown to provide support comparable to, or exceeding, feedback from star formation. This additional heating can reshape the disk thermodynamics and surface-density profile, as well as the expected number density of embedded objects (S. Gilbaum & N. C. Stone 2022; M. Epstein-Martin et al. 2025). Beyond setting the disk structure, the mass and number density of embedded bodies contribute to an effective turbulent viscosity. Strong turbulence can modify migration torques – introducing stochastic kicks – so that trajectories resemble a random walk rather than smoother Type-I/II drift (C. Baruteau & D. N. C. Lin 2010). Indeed, Y. Wu et al. (2024) find that for  $\alpha_{\text{disk}} \gtrsim 0.1$ , turbulent torques dominate.

Environmental factors – such as gas metallicity, opacity prescriptions, and non-axisymmetric gravitational structure from spiral arms or bars – also alter AGN disk profiles. For example, an enhanced effective viscosity due to external torques tends to lower  $\Sigma$ , which in turn

weakens turbulent diffusion and can promote MMR stability. Quantifying these effects in AGN conditions remains an open problem. We regard a systematic exploration as important future work but beyond the scope of this paper.

Beyond the disk physics considered above, migration of embedded bodies can independently restructure the disk density profile. In particular, sufficiently massive perturbers open gaps that decouple them from the local disk environment, suppressing thermal torques. We do not impose this criterion in our analysis, but note that the threshold mass is sensitive to both  $\alpha_{\text{disk}}$  and the MBH mass  $M$ . [S. Gilbaum et al. \(2025\)](#) find that for  $\alpha_{\text{disk}} = 0.01$  and  $M = 10^6 M_{\odot}$ , the minimum gap-opening mass can be as low as  $\sim 5 M_{\odot}$ , rising rapidly with  $M$  and peaking at  $\sim 10^3 M_{\odot}$  for  $M \gtrsim 10^8 M_{\odot}$ . Consequently, in regions of parameter space with low  $M$ , our thermal-torque predictions may be inapplicable, and a Type-I/II torque prescription is more appropriate. For BHs formed in situ in the outer disk, the absence of thermal torques suggest that embedded BHs will migrate inward through the migration trap without encountering other stellar mass objects – unless some originate at small radii and are migrating outwards.

In constructing the Hamiltonian to describe the dynamics of the MMR, we have made several approximations. We assume the system is compact ( $a_2/a_1 \sim 1.2 - 2$ ), that the two objects in orbital resonance have roughly equal mass ( $m_1 \approx m_2$ ) and thus migrate at roughly equal rates, and that the resonance is first-order (such that the orbital periods  $P_2 : P_1$  are described by the ratio  $k+1 : k$ ). For orbital architectures that do not match these assumptions, the exact dynamics of the resonance will differ from what we describe here. For example, first-order resonances technically don't exist at zero eccentricity ([R. Malhotra & N. Zhang 2020](#)), while in contrast, higher-order resonances ( $k+2 : k$  and beyond) have substantial phase space even at  $e \sim 0$ . Similarly, we consider only two-body resonances in this analysis, but capture of migrating objects into three-body Laplace resonances (e.g., [A. Leleu et al. 2021](#); [D. Weisserman et al. 2023](#)) could also be possible and may be more difficult to break than the two-body resonances ([G. Pucacco 2024](#)). Spin-orbit resonances ([G. Li et al. 2023](#)), ejection resonances ([H. G. Bhaskar et al. 2022](#)), and secular resonances ([H. G. Bhaskar et al. 2023](#)) may add further complexity in the subset of systems where they occur.

Our analysis assumes that, absent dissipation and GR precession, convergent, disk-mediated migration generically yields resonant capture. In reality, capture requires adiabatic evolution: the time to cross the reso-

nance must be longer than the libration period. Even then, capture is intrinsically probabilistic ([K. Batygin 2015](#)). Moreover, beyond outright disruption, embedded objects can escape MMRs via resonant metastability ([P. Goldreich & H. E. Schlichting 2014](#); [K. M. Deck & K. Batygin 2015](#)). Recent simulations suggest that realistic turbulence amplifies this pathway by sustaining high equilibrium eccentricities ([Y.-X. Chen et al. 2025](#)). Taken together, these caveats imply our criteria likely overestimate capture rates, and the true incidence of long-lived MMRs in AGN disks may be lower. A full assessment of these effects in the AGN context remains an important direction for future work.

## 7. CONCLUSION

In this work we map where mean-motion resonances (MMRs) between embedded compact objects can survive in AGN disks by developing analytic prescriptions for resonance breaking under (i) GR precession and, (ii) stochastic forcing due to disk turbulence and stellar flybys. For the former, we find that resonances are intrinsically fragile near the central MBH, wherever the GR-driven differential apsidal precession rate  $\Delta\dot{\omega}_{\text{GR}}$  is greater than the libration frequency of the resonance,  $\omega_{\text{lib}}$ . Setting these two quantities equal yields a breaking radius  $R_{\text{GR}}$  which shifts inward for larger embedded masses ( $m$ ), smaller MBH mass ( $M$ ) and higher order commensurabilities (larger  $k$ ).

We derive a unified stochastic disruption criterion by coupling diffusion (turbulence plus stellar flybys) with migration-driven damping (Type-I/II, GW, and thermal torques), comparing the variance in eccentricity and semi-major axis to the libration width. For diffusion in  $a$ , this analytic framework lets us survey a broad AGN parameter space and reveals three MBH-mass regimes: (i) for  $M \gtrsim 10^{7.5} M_{\odot}$ , stable first-order resonances do not occur; (ii) for  $M \lesssim 10^{6.5} M_{\odot}$ , they are always present; and (iii) for  $10^{6.5} M_{\odot} \lesssim M \lesssim 10^{7.5} M_{\odot}$ , stability depends on system parameters including the disk Eddington ratio  $\dot{m}_{\text{disk}}$ , the summed mass of the embedded objects  $m_1 + m_2$ , and the nuclear cusp slope  $\gamma$ . When they exist, radial stability bands typically lie between an inner anti-trap and an outer trap, i.e. where objects are expected to migrate outward.

Stochastic changes in eccentricity play a secondary role. Under the classic [H. Tanaka & W. R. Ward \(2004\)](#) prescription,  $e$  damps on a timescale short relative to diffusion and its variance remains below the resonant bandwidth. For luminous perturbers, thermal torques can excite  $e$ , but it saturates near the disk aspect ratio ( $H/a$ ), which also remains below the resonance band-

width. Thus the semi-major axis channel still sets the break criterion.

Our results suggest that in high-mass AGN ( $M \gtrsim 10^{7.5} M_{\odot}$ ) convergent migration can proceed toward LVK-band mergers largely unimpeded by capture into resonant chains. In low- and intermediate-mass AGN, stable chains are expected primarily within the outward-migration band carved by thermal torques. There they may suppress orbit crossings, with population-level consequences that depend on whether compact objects originate via *in situ* formation in the outer disk (exterior to traps) or are captured from the inner disk.

We note several important sources of uncertainty in our approach including alternative disk prescriptions, which may impact turbulent diffusion and migration timescales, as both explicitly depend on the disk structure. Moreover, thermal torques require a sufficiently small embedded mass that a gap does not open, as well as a scale hierarchy ( $\lambda < H$ ). The former can break down for small  $M$  and large  $m$  while the latter breaks down at large radii. If thermal torques are suppressed, the problem reverts toward Type-I/II-like behavior and MMRs become much less robust – persisting only in small islands at intermediate  $M$  and  $a$ . It is also worth

noting the analytic nature of our work, which should be checked by numerical simulations. As this paper was being completed, we became aware of a forthcoming investigation (Moncrieff & Grishin *in prep*) which examines similar questions about embedded BH dynamics through numerical orbit integration.

While uncertainties in present AGN disk models preclude precise forecasts of merger suppression by MMRs, our criteria and instability maps offer insight into how embedded populations evolve and identify where resonant stabilization is likely. We offer these results as a baseline for future, more detailed modeling that folds in more realistic disk hydrodynamics, torque prescriptions, and diffusion calibrations as those inputs improve.

## ACKNOWLEDGMENTS

We thank Fred Adams and Konstantin Batygin for useful conversations. M.E.M gratefully acknowledges support from *GFSD*. The collaboration visit that started this work was supported by the Wisconsin Alumni Research Foundation, Award #AAM3428. N.C.S. gratefully acknowledges support from the Israel Science Foundation (Individual Research Grant No. 2414/23)

## REFERENCES

Abbott, B. P., Abbott, R., Abbott, T. D., et al. 2016, *PhRvL*, 116, 061102, doi: [10.1103/PhysRevLett.116.061102](https://doi.org/10.1103/PhysRevLett.116.061102)

Abbott, R., Abbott, T. D., Acernese, F., et al. 2023, *Physical Review X*, 13, 041039, doi: [10.1103/PhysRevX.13.041039](https://doi.org/10.1103/PhysRevX.13.041039)

Adams, F. C., & Laughlin, G. 2006, *International Journal of Modern Physics D*, 15, 2133, doi: [10.1142/S0218271806009479](https://doi.org/10.1142/S0218271806009479)

Adams, F. C., Laughlin, G., & Bloch, A. M. 2008, *ApJ*, 683, 1117, doi: [10.1086/589986](https://doi.org/10.1086/589986)

Amaro-Seoane, P. 2018, *Living Reviews in Relativity*, 21, 4, doi: [10.1007/s41114-018-0013-8](https://doi.org/10.1007/s41114-018-0013-8)

Amaro-Seoane, P., Brem, P., Cuadra, J., & Armitage, P. J. 2012, *ApJL*, 744, L20, doi: [10.1088/2041-8205/744/2/L20](https://doi.org/10.1088/2041-8205/744/2/L20)

Amaro-Seoane, P., Andrews, J., Arca Sedda, M., et al. 2023, *Living Reviews in Relativity*, 26, 2, doi: [10.1007/s41114-022-00041-y](https://doi.org/10.1007/s41114-022-00041-y)

Antonini, F., & Perets, H. B. 2012, *ApJ*, 757, 27, doi: [10.1088/0004-637X/757/1/27](https://doi.org/10.1088/0004-637X/757/1/27)

Antonini, F., Toonen, S., & Hamers, A. S. 2017, *ApJ*, 841, 77, doi: [10.3847/1538-4357/aa6f5e](https://doi.org/10.3847/1538-4357/aa6f5e)

Bahcall, J. N., & Wolf, R. A. 1976, *ApJ*, 209, 214, doi: [10.1086/154711](https://doi.org/10.1086/154711)

Barsanti, S., Maselli, A., Sotiriou, T. P., & Gualtieri, L. 2023, *PhRvL*, 131, 051401, doi: [10.1103/PhysRevLett.131.051401](https://doi.org/10.1103/PhysRevLett.131.051401)

Bartko, H., Martins, F., Trippe, S., et al. 2010, *ApJ*, 708, 834, doi: [10.1088/0004-637X/708/1/834](https://doi.org/10.1088/0004-637X/708/1/834)

Bartos, I., Kocsis, B., Haiman, Z., & Márka, S. 2017, *ApJ*, 835, 165, doi: [10.3847/1538-4357/835/2/165](https://doi.org/10.3847/1538-4357/835/2/165)

Baruteau, C., & Lin, D. N. C. 2010, *ApJ*, 709, 759, doi: [10.1088/0004-637X/709/2/759](https://doi.org/10.1088/0004-637X/709/2/759)

Batygin, K. 2015, *MNRAS*, 451, 2589, doi: [10.1093/mnras/stv1063](https://doi.org/10.1093/mnras/stv1063)

Batygin, K., & Adams, F. C. 2017, *AJ*, 153, 120, doi: [10.3847/1538-3881/153/3/120](https://doi.org/10.3847/1538-3881/153/3/120)

Batygin, K., & Brown, M. E. 2010, *ApJ*, 716, 1323, doi: [10.1088/0004-637X/716/2/1323](https://doi.org/10.1088/0004-637X/716/2/1323)

Batygin, K., & Morbidelli, A. 2013, *A&A*, 556, A28, doi: [10.1051/0004-6361/201220907](https://doi.org/10.1051/0004-6361/201220907)

Belczynski, K., Holz, D. E., Bulik, T., & O’Shaughnessy, R. 2016, *Nature*, 534, 512, doi: [10.1038/nature18322](https://doi.org/10.1038/nature18322)

Bellovary, J. M., Mac Low, M.-M., McKernan, B., & Ford, K. E. S. 2016, *ApJL*, 819, L17, doi: [10.3847/2041-8205/819/2/L17](https://doi.org/10.3847/2041-8205/819/2/L17)

Benítez-Llambay, P., Masset, F., Koenigsberger, G., & Szulágyi, J. 2015, *Nature*, 520, 63, doi: [10.1038/nature14277](https://doi.org/10.1038/nature14277)

Bhaskar, H. G., Li, G., & Lin, D. 2023, *ApJ*, 952, 98, doi: [10.3847/1538-4357/acda8f](https://doi.org/10.3847/1538-4357/acda8f)

Bhaskar, H. G., Li, G., & Lin, D. N. C. 2022, *ApJ*, 934, 141, doi: [10.3847/1538-4357/ac7b26](https://doi.org/10.3847/1538-4357/ac7b26)

Bonga, B., Yang, H., & Hughes, S. A. 2019, *PhRvL*, 123, 101103, doi: [10.1103/PhysRevLett.123.101103](https://doi.org/10.1103/PhysRevLett.123.101103)

Cardoso, V., Destounis, K., Duque, F., Macedo, R. P., & Maselli, A. 2022, *PhRvL*, 129, 241103, doi: [10.1103/PhysRevLett.129.241103](https://doi.org/10.1103/PhysRevLett.129.241103)

Chen, Y.-X., Wu, Y., Li, Y.-P., et al. 2025, *MNRAS*, 540, 1998, doi: [10.1093/mnras/staf867](https://doi.org/10.1093/mnras/staf867)

Chrenko, O., Brož, M., & Lambrechts, M. 2017, *A&A*, 606, A114, doi: [10.1051/0004-6361/201731033](https://doi.org/10.1051/0004-6361/201731033)

Coward, D. M., Howell, E. J., Piran, T., et al. 2012, *MNRAS*, 425, 2668, doi: [10.1111/j.1365-2966.2012.21604.x](https://doi.org/10.1111/j.1365-2966.2012.21604.x)

Cresswell, P., & Nelson, R. P. 2008, *A&A*, 482, 677, doi: [10.1051/0004-6361:20079178](https://doi.org/10.1051/0004-6361:20079178)

Deck, K. M., & Batygin, K. 2015, *ApJ*, 810, 119, doi: [10.1088/0004-637X/810/2/119](https://doi.org/10.1088/0004-637X/810/2/119)

Deck, K. M., Payne, M., & Holman, M. J. 2013, *ApJ*, 774, 129, doi: [10.1088/0004-637X/774/2/129](https://doi.org/10.1088/0004-637X/774/2/129)

Derdzinski, A., & Mayer, L. 2023, *MNRAS*, 521, 4522, doi: [10.1093/mnras/stad749](https://doi.org/10.1093/mnras/stad749)

Duffell, P. C., Haiman, Z., MacFadyen, A. I., D’Orazio, D. J., & Farris, B. D. 2014, *ApJL*, 792, L10, doi: [10.1088/2041-8205/792/1/L10](https://doi.org/10.1088/2041-8205/792/1/L10)

Eklund, H., & Masset, F. S. 2017, *MNRAS*, 469, 206, doi: [10.1093/mnras/stx856](https://doi.org/10.1093/mnras/stx856)

Epstein-Martin, M., Tagawa, H., Haiman, Z., & Perna, R. 2025, *MNRAS*, 537, 3396, doi: [10.1093/mnras/staf237](https://doi.org/10.1093/mnras/staf237)

Fromenteau, S., & Masset, F. S. 2019, *MNRAS*, 485, 5035, doi: [10.1093/mnras/stz718](https://doi.org/10.1093/mnras/stz718)

Gangardt, D., Trani, A. A., Bonnerot, C., & Gerosa, D. 2024, *MNRAS*, 530, 3689, doi: [10.1093/mnras/stae1117](https://doi.org/10.1093/mnras/stae1117)

Generozov, A., & Perets, H. B. 2023, *MNRAS*, 522, 1763, doi: [10.1093/mnras/stad1016](https://doi.org/10.1093/mnras/stad1016)

Gerling-Dunsmore, H. J., Begelman, M. C., Simon, J. B., & Armitage, P. J. 2025, arXiv e-prints, arXiv:2508.16842, doi: [10.48550/arXiv.2508.16842](https://doi.org/10.48550/arXiv.2508.16842)

Gilbaum, S., Grishin, E., Stone, N. C., & Mandel, I. 2025, *ApJL*, 982, L13, doi: [10.3847/2041-8213/adb7dc](https://doi.org/10.3847/2041-8213/adb7dc)

Gilbaum, S., & Stone, N. C. 2022, *ApJ*, 928, 191, doi: [10.3847/1538-4357/ac4ded](https://doi.org/10.3847/1538-4357/ac4ded)

Goldreich, P., & Schlichting, H. E. 2014, *AJ*, 147, 32, doi: [10.1088/0004-6256/147/2/32](https://doi.org/10.1088/0004-6256/147/2/32)

Goldreich, P., & Tremaine, S. 1979, *ApJ*, 233, 857, doi: [10.1086/157448](https://doi.org/10.1086/157448)

Goldreich, P., & Tremaine, S. 1980, *ApJ*, 241, 425, doi: [10.1086/158356](https://doi.org/10.1086/158356)

Gondán, L., & Kocsis, B. 2022, *MNRAS*, 515, 3299, doi: [10.1093/mnras/stac1985](https://doi.org/10.1093/mnras/stac1985)

Grishin, E., Gilbaum, S., & Stone, N. C. 2024, *MNRAS*, 530, 2114, doi: [10.1093/mnras/stae828](https://doi.org/10.1093/mnras/stae828)

Guilera, O. M., Miller Bertolami, M. M., Masset, F., et al. 2021, *MNRAS*, 507, 3638, doi: [10.1093/mnras/stab2371](https://doi.org/10.1093/mnras/stab2371)

Hadden, S. 2019, *AJ*, 158, 238, doi: [10.3847/1538-3881/ab5287](https://doi.org/10.3847/1538-3881/ab5287)

Hankla, A. M., Jiang, Y.-F., & Armitage, P. J. 2020, *ApJ*, 902, 50, doi: [10.3847/1538-4357/abb4df](https://doi.org/10.3847/1538-4357/abb4df)

Henrard, J. 1982, *Celestial Mechanics*, 27, 3, doi: [10.1007/BF01228946](https://doi.org/10.1007/BF01228946)

Henrard, J., & Lemaître, A. 1983, *Celestial Mechanics*, 30, 197, doi: [10.1007/BF01234306](https://doi.org/10.1007/BF01234306)

Hopkins, P. F., Squire, J., Su, K.-Y., et al. 2024, *The Open Journal of Astrophysics*, 7, 19, doi: [10.21105/astro.2310.04506](https://doi.org/10.21105/astro.2310.04506)

Hopman, C., & Alexander, T. 2005, *ApJ*, 629, 362, doi: [10.1086/431475](https://doi.org/10.1086/431475)

Inayoshi, K., Tamanini, N., Caprini, C., & Haiman, Z. 2017, *PhRvD*, 96, 063014, doi: [10.1103/PhysRevD.96.063014](https://doi.org/10.1103/PhysRevD.96.063014)

Jiménez, M. A., & Masset, F. S. 2017, *MNRAS*, 471, 4917, doi: [10.1093/mnras/stx1946](https://doi.org/10.1093/mnras/stx1946)

Johnson, E. T., Goodman, J., & Menou, K. 2006, *ApJ*, 647, 1413, doi: [10.1086/505462](https://doi.org/10.1086/505462)

Kanagawa, K. D., Tanaka, H., & Szuszkiewicz, E. 2018, *ApJ*, 861, 140, doi: [10.3847/1538-4357/aac8d9](https://doi.org/10.3847/1538-4357/aac8d9)

Kocsis, B., Yunes, N., & Loeb, A. 2011, *PhRvD*, 84, 024032, doi: [10.1103/PhysRevD.84.024032](https://doi.org/10.1103/PhysRevD.84.024032)

Lauer, T. R., Faber, S. M., Gebhardt, K., et al. 2005, *AJ*, 129, 2138, doi: [10.1086/429565](https://doi.org/10.1086/429565)

Lega, E., Crida, A., Bitsch, B., & Morbidelli, A. 2014, *MNRAS*, 440, 683, doi: [10.1093/mnras/stu304](https://doi.org/10.1093/mnras/stu304)

Leleu, A., Alibert, Y., Hara, N. C., et al. 2021, *A&A*, 649, A26, doi: [10.1051/0004-6361/202039767](https://doi.org/10.1051/0004-6361/202039767)

Levin, Y. 2003, arXiv e-prints, astro. <https://arxiv.org/abs/astro-ph/0307084>

Levin, Y. 2007, *MNRAS*, 374, 515, doi: [10.1111/j.1365-2966.2006.11155.x](https://doi.org/10.1111/j.1365-2966.2006.11155.x)

Li, G., Bhaskar, H. G., Kocsis, B., & Lin, D. N. C. 2023, *ApJ*, 950, 48, doi: [10.3847/1538-4357/acccf1](https://doi.org/10.3847/1538-4357/acccf1)

Lin, D. N. C., & Papaloizou, J. 1986, *ApJ*, 309, 846, doi: [10.1086/164653](https://doi.org/10.1086/164653)

Lu, J. R., Do, T., Ghez, A. M., et al. 2013, *ApJ*, 764, 155, doi: [10.1088/0004-637X/764/2/155](https://doi.org/10.1088/0004-637X/764/2/155)

Luo, J., Chen, L.-S., Duan, H.-Z., et al. 2016, Classical and Quantum Gravity, 33, 035010, doi: [10.1088/0264-9381/33/3/035010](https://doi.org/10.1088/0264-9381/33/3/035010)

Malhotra, R. 1995, AJ, 110, 420, doi: [10.1086/117532](https://doi.org/10.1086/117532)

Malhotra, R., & Zhang, N. 2020, MNRAS, 496, 3152, doi: [10.1093/mnras/staa1751](https://doi.org/10.1093/mnras/staa1751)

Mandel, I., & de Mink, S. E. 2016, MNRAS, 458, 2634, doi: [10.1093/mnras/stw379](https://doi.org/10.1093/mnras/stw379)

Martini, P., & Weinberg, D. H. 2001, The Astrophysical Journal, 547, 12–26, doi: [10.1086/318331](https://doi.org/10.1086/318331)

Masset, F. S. 2017a, MNRAS, 472, 4204, doi: [10.1093/mnras/stx2271](https://doi.org/10.1093/mnras/stx2271)

Masset, F. S. 2017b, MNRAS, 472, 4204, doi: [10.1093/mnras/stx2271](https://doi.org/10.1093/mnras/stx2271)

McKernan, B., Ford, K. E. S., Kocsis, B., Lyra, W., & Winter, L. M. 2014, MNRAS, 441, 900, doi: [10.1093/mnras/stu553](https://doi.org/10.1093/mnras/stu553)

McKernan, B., Ford, K. E. S., Lyra, W., & Perets, H. B. 2012, MNRAS, 425, 460, doi: [10.1111/j.1365-2966.2012.21486.x](https://doi.org/10.1111/j.1365-2966.2012.21486.x)

Meiron, Y., Kocsis, B., & Loeb, A. 2017, ApJ, 834, 200, doi: [10.3847/1538-4357/834/2/200](https://doi.org/10.3847/1538-4357/834/2/200)

Migaszewski, C., & Goździewski, K. 2009, MNRAS, 392, 2, doi: [10.1111/j.1365-2966.2008.14025.x](https://doi.org/10.1111/j.1365-2966.2008.14025.x)

Morbidelli, A., & Crida, A. 2007, Icarus, 191, 158, doi: [10.1016/j.icarus.2007.04.001](https://doi.org/10.1016/j.icarus.2007.04.001)

Murray, C. D., & Dermott, S. F. 1999, Solar System Dynamics (Cambridge, UK: Cambridge University Press), doi: [10.1017/CBO9781139174817](https://doi.org/10.1017/CBO9781139174817)

Oishi, J. S., Mac Low, M.-M., & Menou, K. 2007, ApJ, 670, 805, doi: [10.1086/521781](https://doi.org/10.1086/521781)

Okuzumi, S., & Ormel, C. W. 2013, ApJ, 771, 43, doi: [10.1088/0004-637X/771/1/43](https://doi.org/10.1088/0004-637X/771/1/43)

Paardekooper, S. J., Baruteau, C., Crida, A., & Kley, W. 2010, MNRAS, 401, 1950, doi: [10.1111/j.1365-2966.2009.15782.x](https://doi.org/10.1111/j.1365-2966.2009.15782.x)

Paardekooper, S.-J., Rein, H., & Kley, W. 2013, MNRAS, 434, 3018, doi: [10.1093/mnras/stt1224](https://doi.org/10.1093/mnras/stt1224)

Pan, Z., Lyu, Z., & Yang, H. 2021, PhRvD, 104, 063007, doi: [10.1103/PhysRevD.104.063007](https://doi.org/10.1103/PhysRevD.104.063007)

Pan, Z., Lyu, Z., & Yang, H. 2022, PhRvD, 105, 083005, doi: [10.1103/PhysRevD.105.083005](https://doi.org/10.1103/PhysRevD.105.083005)

Pan, Z., & Yang, H. 2021, PhRvD, 103, 103018, doi: [10.1103/PhysRevD.103.103018](https://doi.org/10.1103/PhysRevD.103.103018)

Peng, P., Franchini, A., Bonetti, M., Sesana, A., & Chen, X. 2025, ApJ, 989, 122, doi: [10.3847/1538-4357/ade42](https://doi.org/10.3847/1538-4357/ade42)

Peters, P. C. 1964, Physical Review, 136, 1224, doi: [10.1103/PhysRev.136.B1224](https://doi.org/10.1103/PhysRev.136.B1224)

Portegies Zwart, S. F., & McMillan, S. L. W. 2000, ApJL, 528, L17, doi: [10.1086/312422](https://doi.org/10.1086/312422)

Pucacco, G. 2024, Celestial Mechanics and Dynamical Astronomy, 136, 51, doi: [10.1007/s10569-024-10221-3](https://doi.org/10.1007/s10569-024-10221-3)

Quillen, A. C. 2006, MNRAS, 365, 1367, doi: [10.1111/j.1365-2966.2005.09826.x](https://doi.org/10.1111/j.1365-2966.2005.09826.x)

Quillen, A. C. 2011, MNRAS, 418, 1043, doi: [10.1111/j.1365-2966.2011.19555.x](https://doi.org/10.1111/j.1365-2966.2011.19555.x)

Rein, H., & Papaloizou, J. C. B. 2009, A&A, 497, 595, doi: [10.1051/0004-6361/200811330](https://doi.org/10.1051/0004-6361/200811330)

Reved, O., Friedland, L., & Stone, N. C. 2025, MNRAS, 537, 661, doi: [10.1093/mnras/staf051](https://doi.org/10.1093/mnras/staf051)

Richardson, D. L., & Kelly, T. J. 1988, Celestial Mechanics, 43, 193, doi: [10.1007/BF01234566](https://doi.org/10.1007/BF01234566)

Rodriguez, C. L., Chatterjee, S., & Rasio, F. A. 2016, PhRvD, 93, 084029, doi: [10.1103/PhysRevD.93.084029](https://doi.org/10.1103/PhysRevD.93.084029)

Rowan, C., Boekholt, T., Kocsis, B., & Haiman, Z. 2023, MNRAS, 524, 2770, doi: [10.1093/mnras/stad1926](https://doi.org/10.1093/mnras/stad1926)

Ruan, W.-H., Guo, Z.-K., Cai, R.-G., & Zhang, Y.-Z. 2020, International Journal of Modern Physics A, 35, 2050075, doi: [10.1142/S0217751X2050075X](https://doi.org/10.1142/S0217751X2050075X)

Sano, T., Inutsuka, S.-i., Turner, N. J., & Stone, J. M. 2004, ApJ, 605, 321, doi: [10.1086/382184](https://doi.org/10.1086/382184)

Secunda, A., Bellovary, J., Mac Low, M.-M., et al. 2019, ApJ, 878, 85, doi: [10.3847/1538-4357/ab20ca](https://doi.org/10.3847/1538-4357/ab20ca)

Secunda, A., Hernandez, B., Goodman, J., et al. 2021, ApJL, 908, L27, doi: [10.3847/2041-8213/abe11d](https://doi.org/10.3847/2041-8213/abe11d)

Secunda, A., Bellovary, J., Mac Low, M.-M., et al. 2020, ApJ, 903, 133, doi: [10.3847/1538-4357/abbc1d](https://doi.org/10.3847/1538-4357/abbc1d)

Sessin, W., & Ferraz-Mello, S. 1984, Celestial Mechanics, 32, 307, doi: [10.1007/BF01229087](https://doi.org/10.1007/BF01229087)

Seto, N., & Muto, T. 2010, PhRvD, 81, 103004, doi: [10.1103/PhysRevD.81.103004](https://doi.org/10.1103/PhysRevD.81.103004)

Shakura, N. I., & Sunyaev, R. A. 1973, A&A, 24, 337

Shlosman, I., & Begelman, M. C. 1989, ApJ, 341, 685, doi: [10.1086/167526](https://doi.org/10.1086/167526)

Sirko, E., & Goodman, J. 2003, MNRAS, 341, 501, doi: [10.1046/j.1365-8711.2003.06431.x](https://doi.org/10.1046/j.1365-8711.2003.06431.x)

Stone, N. C., & Metzger, B. D. 2016, MNRAS, 455, 859, doi: [10.1093/mnras/stv2281](https://doi.org/10.1093/mnras/stv2281)

Stone, N. C., Metzger, B. D., & Haiman, Z. 2017, MNRAS, 464, 946, doi: [10.1093/mnras/stw2260](https://doi.org/10.1093/mnras/stw2260)

Tagawa, H., Haiman, Z., & Kocsis, B. 2020, ApJ, 898, 25, doi: [10.3847/1538-4357/ab9b8c](https://doi.org/10.3847/1538-4357/ab9b8c)

Tagawa, H., Kocsis, B., Haiman, Z., et al. 2021, ApJ, 908, 194, doi: [10.3847/1538-4357/abd555](https://doi.org/10.3847/1538-4357/abd555)

Tamayo, D., & Hadden, S. 2025, ApJ, 986, 11, doi: [10.3847/1538-4357/adclc4](https://doi.org/10.3847/1538-4357/adclc4)

Tanaka, H., & Ward, W. R. 2004, ApJ, 602, 388, doi: [10.1086/380992](https://doi.org/10.1086/380992)

The LIGO Scientific Collaboration, the Virgo Collaboration, the KAGRA Collaboration, et al. 2025, arXiv e-prints, arXiv:2508.18082, doi: [10.48550/arXiv.2508.18082](https://doi.org/10.48550/arXiv.2508.18082)

Thompson, T. A., Quataert, E., & Murray, N. 2005, ApJ, 630, 167, doi: [10.1086/431923](https://doi.org/10.1086/431923)

Toomre, A. 1964, ApJ, 139, 1217, doi: [10.1086/147861](https://doi.org/10.1086/147861)

Tutukov, A. V., & Yungelson, L. R. 1993, MNRAS, 260, 675, doi: [10.1093/mnras/260.3.675](https://doi.org/10.1093/mnras/260.3.675)

van Son, L. A. C., de Mink, S. E., Renzo, M., et al. 2022, ApJ, 940, 184, doi: [10.3847/1538-4357/ac9b0a](https://doi.org/10.3847/1538-4357/ac9b0a)

Velasco Romero, D. A., & Masset, F. S. 2020, MNRAS, 495, 2063, doi: [10.1093/mnras/staa1215](https://doi.org/10.1093/mnras/staa1215)

Volpi, M., & Libert, A.-S. 2024, A&A, 683, A193, doi: [10.1051/0004-6361/202346727](https://doi.org/10.1051/0004-6361/202346727)

Wang, Y., Zhu, Z., & Lin, D. N. C. 2024, MNRAS, 528, 4958, doi: [10.1093/mnras/stae321](https://doi.org/10.1093/mnras/stae321)

Ward, W. R. 1997, Icarus, 126, 261, doi: [10.1006/icar.1996.5647](https://doi.org/10.1006/icar.1996.5647)

Weisserman, D., Becker, J. C., & Vanderburg, A. 2023, AJ, 165, 89, doi: [10.3847/1538-3881/acac80](https://doi.org/10.3847/1538-3881/acac80)

Wisdom, J. 1986, Celestial Mechanics, 38, 175, doi: [10.1007/BF01230429](https://doi.org/10.1007/BF01230429)

Wu, Y., Chen, Y.-X., & Lin, D. N. C. 2024, MNRAS, 528, L127, doi: [10.1093/mnrasl/slad183](https://doi.org/10.1093/mnrasl/slad183)

Xu, W.-L., Li, Y.-Z., Chen, Y.-G., Li, H., & Lei, W.-H. 2025, arXiv e-prints, arXiv:2505.07114, doi: [10.48550/arXiv.2505.07114](https://doi.org/10.48550/arXiv.2505.07114)

Yang, H., & Casals, M. 2017, PhRvD, 96, 083015, doi: [10.1103/PhysRevD.96.083015](https://doi.org/10.1103/PhysRevD.96.083015)

Yang, Y., Bartos, I., Gayathri, V., et al. 2019, PhRvL, 123, 181101, doi: [10.1103/PhysRevLett.123.181101](https://doi.org/10.1103/PhysRevLett.123.181101)

Yunes, N., Kocsis, B., Loeb, A., & Haiman, Z. 2011, PhRvL, 107, 171103, doi: [10.1103/PhysRevLett.107.171103](https://doi.org/10.1103/PhysRevLett.107.171103)